CRITICAL REVIEW

Check for updates

Layered double hydroxides (LDH) materials for effective phosphate adsorption from aqueous solution

Catalina V. Flores, [a] Juan L. Obeso, *[b] Leonardo Herrera-Zuñiga,[c] Ricardo A. Peralta, [d] J. Israel Campero-Domínguez,[e] Leobardo Morales-Ruiz,[b] Nora S. Portillo-Vélez *[de] and Juan Carlos Valdivia-Corona*[b]

Water eutrophication caused by excess nutrients can be addressed by applying layered double hydroxide (LDH) materials. The LDH structure is based on positively charged layers and negatively charged counterions between the layers, or solvent molecules, which are optimal for phosphate removal. The $M^{2+}:M^{3+}$ molar ratio and the synthesis method employed affect LDH properties. LDH materials are synthesized using co-precipitation, urea hydrolysis, hydrothermal treatment, and sol–gel methods. The phosphate adsorption performance of different LDH materials is compared, focusing on Al, Fe, and La, as well as Zn, Mg, and Ca. The role of LDH composites is highlighted. Different optimization parameters, including dosage, contact time, pH, initial concentration, reusability, temperature, and the influence of co-existing ions, are discussed. Interactions such as electrostatic attraction (ES), ion exchange (IX), ligand exchange (LX), ligand complexation (LC), surface complexation (SC), hydrogen bonding (HB), and $\pi-\pi$ appear to be the main mechanisms of phosphate adsorption by LDHs. Thus, the need for low-cost and efficient systems for phosphate recycling underscores the promise of tunable LDH composition for selective phosphate adsorption as LDH materials have demonstrated sustained performance, verifiable regeneration, successful real-world piloting, scalable supply, and regulatory standards consistent with the circular economy.

Sustainability spotlight

Ensure availability and sustainable management of water and sanitation for all. This project aligns with one of the 17 Sustainable Development Goals of the United Nations. Water pollution has discriminately increased over the last decade due to the negative environmental impact generated by current civilization. The most alarming water pollutants are organic dyes, heavy metals, pharmaceuticals, fluoride, and nutrients, as the presence of all these pollutants can have devastating consequences for both human health and the environment. Notably, nutrient contamination has recently garnered increased attention due to its significant impact on various aquatic systems. The nutrients are directly associated with nitrogen and phosphorus, which are key factors in the eutrophication process. In general, eutrophication is the enrichment of a water body with essential nutrients, leading to an accelerated rate of photosynthesis and increased growth of aquatic plants, which can result in algal blooms, diminished water transparency, and oxygen depletion.

[a]Instituto Politécnico Nacional, CICATA U. Legaria, Laboratorio Nacional de Ciencia, Tecnología y Gestión Integrada del Agua (LNAgua), Legaria 694, Col. Irrigación, Miguel Hidalgo, 11500, CDMX, Mexico

[b]División de Ingeniería en Sistemas Automotrices, Tecnológico de Estudios Superiores del Oriente del Estado de México, Tecnológico Nacional de México, Estado de México 56400, Mexico. E-mail: juan.so@otemexico.tecnm.mx; juan.valdivia@tesoem.edu.mx

[c]Departamento de Ciencias Naturales, Universidad Autonoma Metropolitana Unidad Cuajimalpa, Ciudad de México, Mexico

[d]Departamento de Química, División de Ciencias Básicas e Ingeniería. Universidad Autónoma Metropolitana (UAM-I), 09340, Mexico. E-mail: noraportillo@xanum. uam.mx

[e]División de Investigación y posgrado, Tecnológico de Estudios Superiores del Oriente del Estado de México, Tecnológico Nacional de México, Estado de México 56400, Mexico

1. Introduction

Water pollution has discriminately increased over the last decade due to the negative environmental impact generated by current civilization. Due to industrial, agricultural, and mining activities, a high number of pollutants have been discharged into various water bodies, specifically into rivers, lakes, and oceans.[1] The most alarming water pollutants are organic dyes, heavy metals, pharmaceuticals, fluoride, and nutrients, as the presence of all these pollutants can have devastating consequences for both human health and the environment.[2] Specifically, nutrient contamination has recently garnered more attention because it has significantly impacted various aquatic systems. The nutrients are directly associated with nitrogen and

phosphorus, which are key factors in the process of eutrophication. In general, eutrophication is the enrichment of a water body with essential nutrients, leading to an accelerated rate of photosynthesis and increased growth of aquatic plants, which can result in algal blooms, diminished water transparency, and oxygen depletion.[3]

Phosphorus management and control have been enhanced in various countries, including Mexico and the US, due to the excessive accumulation of phosphate ions in water. Phosphorus is a vital nutrient for food production and is widely used as a fertilizer in agriculture.[4,5] It was found that in some water systems, the phosphate discharged surpassed the permissible levels, with concentrations higher than 15 mg L^{-1}.[6] Long-term accumulation can compromise food sustainability and the safety of agricultural practices. Therefore, it is necessary to address these problems, as they are crucial for a sustainable farming future.[7] Different strategies for phosphate management based on phosphate recovery have been implemented as an optimal solution. Almost 85% of phosphate is collected by industrial processes; however, its use is limited due to the presence of interfering and hazardous ions. The implementation of selective phosphate ion separation techniques is needed.[8]

Structured materials have been applied as an alternative for selective phosphate adsorption from water solutions. These include metal–organic frameworks,[9] metal-coordinated, amino-functionalized silicas, ammonium-functionalized silicas, metal-doped mesoporous silicas,[10] and activated carbons.[11] Unfortunately, these materials are hindered by intricate sample processing, costly instrumentation, and toxic solvents, since it is necessary to design low-cost materials for phosphate removal. Based on this, layered double hydroxide (LDH) materials can be a functional option due to their versatile processing.[12] LDH materials exhibit a layered structure, which is formed by positively charged metal hydroxide layers and negatively charged anions intercalated between the layers. The LDH composition can be tuned by modifying the metal cations and anions during the synthesis process. For the layers, the void between each layer can be designed for a specific application, which can be related to an adsorption process. The main properties are anion exchange (AX), high surface area, thermal, chemical, and mechanical stability, and biocompatibility[13,14]

LDH materials have been used as catalysts,[15] for drug delivery,[16] for gas adsorption,[17] and for photocatalytic water splitting.[13] For water pollutants removal, LDH materials have displayed high properties for removing pharmaceuticals,[18] organic dyes,[19] and heavy metals.[20] The outstanding performance of LDH materials paves the way for water pollution treatment. Moreover, the chemical structure of LDH facilitates the AX process, highlighting its application in nutrient recovery due to the phosphate molecule's negative charge. Based on this, this review aims to establish the role of LDH materials in selective phosphate adsorption applications by capitalizing on the primary contribution to this topic. The type of adsorption mechanism between the phosphate molecule and the LDH materials has been discussed. The chemical properties and

maximum adsorption capacity of the material have been mentioned.

2. Structure of LDH materials

LDH materials, with the common name of hydrotalcite, are a class of clay minerals forming ionic lamellar compounds. The general formula of LDH materials is $[M^{2+}_{1-x}M^{3+}_x(OH)_2]$ $[A^{n-}]_{x/n} \cdot zH_2O$, where M^{2+} can be a divalent metal center, and Mn^{3+} is a trivalent metal center. A^{n-} is a counterion for the charge compensating, and x is the molar ratio of $M^{3+}/(M^{2+} + M^{3+})$, which is generally between 0.2 and 0.4.[12] LDH materials are based on positive layers and negative counterions between the layers or solvent molecules. This structure forms infinite 2D sheets, with the metal cation in octahedral geometry. This structure is related to the brucite $Mg(OH)_2$ layers, and each cation is surrounded by six OH^- ions that are pointed towards the corners and form infinite sheets (Fig. 1).[21]

In other words, the layers are composed of divalent and trivalent cations binding to OH groups, and between each layer, a negative molecule balances the charge.[13,22]

3. Synthesis of LDH materials

Different strategies have been reported for LDH-based materials synthesis, including (i) co-precipitation, (ii) urea hydrolysis, (iii) hydrothermal, and (iv) sol–gel method (Fig. 2).

3.1 Co-precipitation

Co-precipitation is one of the most widely employed methods for LDH synthesis, due to its scalability and simplicity. It consists of M^{2+} and M^{3+} metal salts dissolved in an aqueous alkaline solution at fixed or varying pH. When co-precipitation is achieved with a lengthy synthesis time of several days, this method yields high-crystalline products. The solution's concentration and molar ratio of bivalent and trivalent salts influence morphological characteristics and particle sizes.[23] LDHs synthesized *via* the co-precipitation method are highly
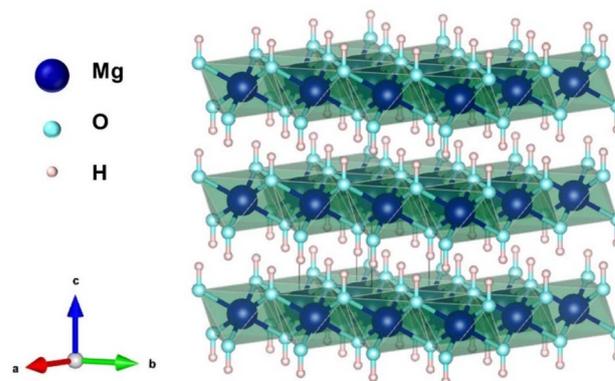

Fig. 1 Crystal structure of brucite ($Mg(OH)_2$) (reprinted with permission from ref. 21 Copyright 2022 MDPI, Basel, Switzerland, under the terms and conditions of the Creative Commons Attribution (CC BY) license).
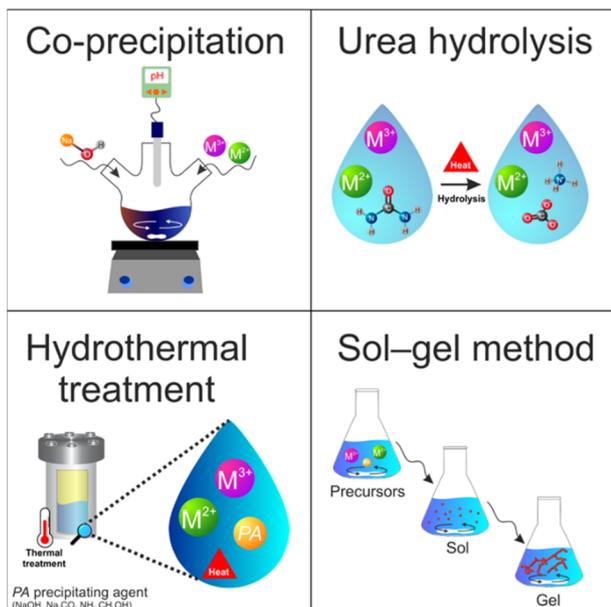
Fig. 2 Schematic representation of diverse strategies for LDH-based materials synthesis.

sensitive to the initial reactant concentrations, as these directly affect the degree of supersaturation in the solution. The relative rates of nucleation and crystal growth govern the relationship between supersaturation and the resulting crystal structure. Grover et al.[24] synthesized an LDH by precipitation, which was applied in the adsorption of anionic dyes. The starch-magnesium/aluminum layered double hydroxide (S-Mg/Al LDH) synthesized showed an adsorption capacity in the order Amaranth > Tartrazine > Sunset Yellow > Eosin Yellow. This method also allows for the remediation of heavy metals from water for LDH formation. In addition to water remediation applications, Zhou et al.[25] utilized Fe@MgAl LDH to detect and quantify bisphenol A, 4-nonylphenol, and 4-octylphenol through solid-phase extraction. The detection limits for the three contaminants were determined to be 0.24–0.34 $\mu g\ L^{-1}$. The result is a simple, fast, sensitive, easy-to-operate method for determining water pollutants.

3.2 Urea hydrolysis

The hydrolysis synthesis method enables improved control over the crystallinity of the product through process conditions, including temperature, $M^{2+}:M^{3+}$ molar ratio, urea concentration, and reaction time.[26] This involves the thermal treatment of precursor salts and a precipitating element mixture using an autoclave. The precipitating agent improves the control and homogeneity of the product's precipitation, crystallization, and size.[27] As a precipitating agent, urea's slow thermal degradation above 90 °C in carbonate, CO_3^{2-}, and ammonia ions generates the alkaline pH necessary for synthesizing LDH.[28] Thus, carbonate is the only interlaminar anion employed. The urea-assisted hydrolysis method was employed to synthesize the MgCoAl and NiCoAl layered double hydroxides (LDHs).

Chagas et al.[29] find that the optimal synthesis conditions are a molar ratio of 1 : 3 $M^{2+}:M^{3+}$, at 120 °C for 24 h, for crystalline materials with a single hydrotalcite-like phase present. However, higher crystals were obtained for MgCoAl samples. Additionally, the interlaminar carbonate anions exhibit stronger intermolecular interactions in MgCoAl samples, as indicated by the cell parameters. This shows a stronger ES attraction between hydroxyls and interlayer carbonate anions. Similarly, Tian et al.[30] synthesized Ni-Fe-based LDH nanospheres by mixing nickel(II) nitrate hexahydrate, $Ni(NO_3)_2\cdot 6H_2O$, and iron(III) nitrate hexahydrate, $Fe(NO_3)_3\cdot 6H_2O$, with urea at 120 °C for 10 h. By adding CoS_2@Ni, the NiFe-LDH was applied to the synthesis of an electrode that exhibits outstanding specific capacitance.

3.3 Hydrothermal treatment

Similar to the urea hydrolysis method, it involves dissolving metal precursors in water and, in some cases, adding precipitating agents such as sodium hydroxide, sodium carbonate, ammonia, urea, and methanol, followed by thermal treatment using an autoclave at high temperatures.[31] The temperature employed is generally below 300 °C and can take several days. Generally, high temperatures and prolonged synthesis periods yield higher amounts of LDHs. Concerning the precursors, numerous organic and inorganic metallic salts can be used. However, this method is most suitable when low-affinity organic precursors, such as organo-anions, are incorporated and intended to be disposed of in the interlamellar space.[32] Analogous to the other methods, the $M^{2+}:M^{3+}$ molar ratio plays a significant role. Thus, it is possible to obtain a wide variety of LDHs. Farghali et al.[33] studied the hydrothermal synthesis and application of MgAl-LDH in the remediation of dye-contaminated water. Employing a molar ratio of 2 : 1, $Mg^{2+}:Al^{3+}$, and NaOH as precipitating agents, they obtained a high crystallinity with pure hydrotalcite phase LDH. The MgAl-LDH exhibited an outstanding adsorption capacity of 769 mg g^{-1} for the widely employed textile dye Congo red. They also note that the primary interaction mechanism is the ES interaction between the MgAl-LDH positively charged surface and the Congo red negatively charged surface.

This method can also enhance other LDH synthesis methods, such as co-precipitation, sol–gel, or urea hydrolysis, to produce higher-quality LDH.[34] Silva et al.[35] evaluated seven different synthesis methods for MgFe/LDH to remove nitrate, antibiotic rifampicin, and hormone 17-α-methyltestosterone from water. Parameters such as phase purity, crystallinity, and textural features were evaluated. The PXRD results demonstrated that co-precipitation at a constant pH, followed by the hydrothermal method, produced a higher crystallinity LDH with the most intense and well-defined peaks. Also, this synthesis method of LDH shows a higher removal of nitrate and 17-α-methyltestosterone.

3.4 Sol–gel method

This method involves a mixture of precursor metal salts dissolved in water or organic solvents at room temperature for an

extended period. In addition to producing high-purity LDHs with controlled pore sizes and high surface areas, this process is distinguished by being low-cost and energy-efficient.[36] It consists of the dissolution and hydrolysis of the alkoxide, forming a sol, which experiences a limited and incomplete condensation of the metallic salts, resulting in a gel.[27] Saikia et al.[37] synthesized a Ni–Al-LDH through the sol–gel method, employing acetylacetonate as a precursor. In another study, Tichit et al.[36] synthesized Zn/Al and Pt/Zn/Al LDHs. They found that employing Zn acetate-2-hydrate or Al acetylacetonate precursor at 273 K resulted in a maximum yield of 50 mol%. However, using Zn acetylacetonate and Al isopropoxide precursors at 273 K, the maximum LDH amount was 90 mol%. They also observed a relationship between synthesis conditions, such as the nature of the precursors and temperature, and the formation of added phases.

4. Phosphate adsorption performance using LDH materials

Phosphate molecules are negative ions with the formula PO_4^{3-}. The geometry exhibits a central phosphorus atom surrounded by four oxygen atoms in a tetrahedral arrangement. Some phosphate salts, including sodium, potassium, rubidium, caesium, and ammonium phosphate, are highly soluble in water at standard conditions, whereas the phosphates of most other metals exhibit low solubility. Phosphate ions are considerably strong bases that can be hydrolyzed in water environments to generate a basic solution. Generally, the presence of phosphate in water contributes to eutrophication. Based on this, it is reported that the maximum phosphorus concentration in lakes and rivers can be 25 and 100 $\mu g\ L^{-1}$.[38] However, a highly concentrated dissolved phosphate was found in a lake.[39] For this, it is necessary to establish alternatives to eliminate the excess phosphate in water. A range of techniques, including biological treatment,[40] chemical precipitation,[41] and adsorption[42] have been employed for phosphate removal from water. Nevertheless, the adsorption process has been widely applied due to its effectiveness and low cost. Different materials have been used for phosphate adsorption from water, such as polymers,[43] metal–organic frameworks,[44] and activated carbons.[11] Distinctively, LDH-based materials have been widely applied to phosphate remediation from aqueous solutions. Due to their versatile tunability, different metal centers, counterions, functionalization, and composites have been used for this purpose.[45–48] A comparison of diverse LDH-based materials is displayed in Table 1.

Then, LDH materials offer distinct advantages for phosphate removal compared to materials such as Metal–Organic Frameworks (MOFs) and Activated Carbons (ACs), primarily due to their unique structure and dominant removal mechanism. The positive charge and ion exchange, the memory effect in the synthesis of LDO materials, and the ease of synthesizing composite materials are highlighted.[81,82] On the other hand, MOFs display high surface areas and structural precision; their high cost, complex synthesis, and limited stability in realistic

wastewater environments often make LDHs a more practical and scalable choice for large-scale water treatment applications focused on phosphate removal.[83]

4.1 M–Al based LDH materials (M = Zn, Mg, Ca)

M–Al-based LDH materials, where M represents a divalent metal such as Zn, Mg, and Ca, have been extensively explored for their effectiveness in phosphate adsorption from aqueous environments. Due to the presence of exchangeable anions in the interlayer region, LDHs exhibit a high AX capacity.[84] The zinc aluminum LDH material is among the most versatile, as it can be synthesized with different Zn/Al molar ratios.[85]

Iftekhar et al.[50] reported an LDH synthesis with a different molar ratio and calcination temperature ZxAy, where x and y represent the molar ratio and calcination temperature, respectively. The molar ratio was from 1 to 4, and the calcination was from 100 to 400 °C. In a screening study, the material noted as Z3A200 LDH displays the highest adsorption for phosphate molecules. This material was tested in various pH environments, exhibiting a decrease in its properties with increasing pH. The experimental data demonstrate a good fit for the Langmuir model at various temperatures (25–55 °C), indicating an adsorption capacity of 2.6–2.72 mmol g^{-1}. Kinetic analysis reveals that a chemisorption process is the controlling step in the macro-pore diffusion of phosphate. A proposed mechanism based on zeta potential, SEM, and EDS analysis was discussed, displaying ES interactions, IX, and LC.

Then, co-precipitation achieved by the urea hydrolysis method is widely used for LDH synthesis.[86–89] For this, a comparison was reported between different synthesis methods for Zn-Al LDH materials with molar ratios of 2 and 3.[49] The impact of phosphate removal from the solution was compared. For the urea hydrolysis synthesis, the materials display similar phosphate adsorption, even with different metal molar ratios, indicating a minimal effect of the varying metal concentrations in the sample. However, the material with a molar ratio of 3 contains CO_3^{2-} and NO_3^{-} species, and the materials with a molar ratio of 2 only contain NO_3^{-} species. For this, an effect on the counterions is observed, as lower phosphate adsorption is reported for the materials with CO_3^{2-} due to its non-exchangeability. Kinetic data were fitted to a pseudo-second order (PSO) model. The experimental data were well-fitted to the Freundlich model, indicating a multi-step adsorption process. The materials show proper selectivity for phosphate ions in the presence of sulfate, bicarbonate, and chloride. Therefore, Seftel et al.[90] reported a structurally modified Zn-Al LDH material with different cationic ratios and interlayer anions. LDHs were synthesized by the co-precipitation method at constant pH. The materials were labeled as Zn_rAl-CO_3, Zn_rAl-NO_3, and $Zn_{1.25}Al-Cl$ (where r represents the Zn/Al cationic ratio). Phosphate adsorption exhibits distinct kinetic behavior at varying Zn/Al molar ratios and with different interlayer anions. The PSO model fits properly for all the materials. The K_2 (PSO model constant) values indicate a fast adsorption in the order of $Zn_{1.25}Al-NO_3 > Zn_{1.5}Al-NO_3 > Zn_2Al-NO_3$. Then, by comparing different interlayer anions (Cl, CO_3, and NO_3) with

Table 1 Comparison of phosphate adsorption in diverse LDH-based materials[a]

LDH base materials	Surface area ($m^2 \ g^{-1}$)	pH	Time (h)	Kinetic model and isotherm adsorption	Phosphate adsorption capacity ($mg \ g^{-1}$)	Mechanism	Ref.
PS-La-LDH	56.07	3–8		PSO Freundlich	34 (P)	ES adsorption LX IX	45
MgFe–Zr LDH @ magnetic particles		4.5–5	1	PSO Langmuir	35		46
Zn_{2G}-Al		6	8	PSO Freundlich	237	AX, SC, and SP	49
Z3A200 LDH	85	4	3	PSO Langmuir	258	ES, LC, and IX	50
Zn–Al LDH	135	2–10	0.6	PSO Langmuir	68	ES, LX, and IX	51
Mg–Al LDH	104	2–6		PSO Freundlich	31		
Mg-Al LDH	1214	5	5	Langmuir	213	AX, ES, and SC	52
CAs-4	7.46	4–10		PSO	126	AX, ES, and dissolution precipitation	53
CA-4	5.96			Langmuir	127		
Mg_2-Al_1-Cl-LDH	13.4	4–6	0.6	PSO Langmuir	76	IX, ES, and LX	54
Biochar/MgAl-LDH			1	PSO Langmuir Langmuir–Freundlich	410		55
MMAL-0.375	47.7	4–10	0.5	PSO Langmuir	66.5 (P)	ES attraction, and LX	56
$SBAC_{100}MgFe$	169	3	4.1	PFO Langmuir	104	ES and IX HB and π–π interactions	57
LDHBC	267	1–11	5	PFO Langmuir and Freundlich	1279	IX	58
NO_3-Hex-LDH		4.5–11			49 (P)	Restacking	59
MCSHT	63.3	5–7	0.5	PSO	39.9	SC, ES, and IX	60
MAlgHT	60.3			Freundlich	29.7		
ML-11	64	4–10	3	PSO Freundlich	121.5	ES, and IX	61
Fe_3O_4@SiO_2@mLDH350	137	3–12		Langmuir	57	SC	62
La-MgFe-LDH/BC	71.6	3–11	1	PSO Langmuir	62.2 (P)	ES, AX, SC, and SP	63
LDH-BMBC	370	3–11		PFO PSO Freundlich	56.2 (P)	AX, ES, SC	64
MBC@LDH		4–9	6	PSO Langmuir		AX, LX, HB	65
Zr-LDH		2–10	6	PSO	99.3		66
Zr-LDO				Langmuir and Freundlich	80.3		
Mg(AlZr)-LDH(CO_3)	<35	4–10		Freundlich	10 (P)	IX	67
B_5MgAl	441	2–12	5	PFO Langmuir	141	SC	68
BR-LDH		2–12	3.3	PSO Freundlich	2.6	ES, IX SC	69
LaCa-LDH/CS	20.5	3–7	8	PSO	149.5 (P)	ES, LX, IX, HB	70
CeCa-LDH/CS	28.1			Freundlich	174.6 (P)		
GO/MgMn-LDH-300	38.6		1.5	PSO	70.8 (P)	LX, IX, ES	71
Mg-Al-CO_3 LDH/Chitosan	28.4	6		PSO Freundlich	106.3	ES	72
BBAC@Zn–Al LDHs	90.5	2–6	0.6	PSO Freundlich	87	ES, SC, and IX	73
$MnFe_2O_4$/ZnFe-LDH	26.9	2–5	4	PSO Freundlich	94.5	AX	74
NiFe-LDH/rGO			6	PSO	270		75
Fe_3O_4/MgAl-NO_3		3–10	2	PSO	33.4 (P)	AX and ES	76

Table 1 (*Contd.*)

LDH base materials	Surface area ($m^2 g^{-1}$)	pH	Time (h)	Kinetic model and isotherm adsorption	Phosphate adsorption capacity ($mg g^{-1}$)	Mechanism	Ref.
Al-Fe$_2$O$_3$/LDH	40.6	2.5–3	0.016	Langmuir PSO	93.06(P)	LX, SC, ES, HB	77
Mg-Fe LDH beads	30.4	5–9	3	Langmuir–Freundlich PSO	2.05 (P)		78
ZrO$_2$/Mg–Fe LDH		≤3	9	Freundlich PSO	35.4 (P)		79
Fe$_3$O$_4$/Zn-Al-Fe-La-LDH	4		24	Freundlich PSO Langmuir	169.5	IX	80

[a] Surface complexation (SC), surface precipitation (SP), electrostatic attraction (ES), ion exchange (IX), anion exchange (AX), ligand exchange (LX), hydrogen bond (HB), and (P) phosphorus adsorption.

the same Zn/Al cationic ratio (1.25), the adsorption equilibrium was higher for Zn$_{1.25}$Al-NO$_3$, suggesting the high affinity for the phosphate molecule. Based on this particular material, the Langmuir model displays a maximum adsorption capacity of 90.91 mg g^{-1}. The sorption mechanism was proposed based on the experimental data and micro-Raman spectroscopy. AX was proposed since phosphate molecules are distributed between the surface hydroxyl groups.

Yu et al.[91] reported a modified Zn–Al LDH material intercalated with pyromellitic acid (PMA). The material was labeled as [Zn$_{0.68}$Al$_{0.32}$(OH)$_2$](PMA)$_{0.08}$·0.3H$_2$O, denoted as Zn$_2$Al-PMA-LDHs. A high selectivity for the phosphate molecule was observed in a hybrid solution containing H$_2$PO$_4^-$, SO$_4^{2-}$, CO$_3^{2-}$, NO$_3^-$, and Cl$^-$. The PSO model drove the kinetics, with a Langmuir maximum adsorption capacity of 64.3 mg g^{-1} at 323 K. The adsorption mechanism was proposed based on FT-IR and XPS analysis. An HB between the hydroxyl group of phosphate, as the donor, and the oxygen of the dissociated aromatic carboxyl group, as the acceptor, was found to play a key role in phosphate adsorption interaction.

Gao et al.[92] reported that Cu^{2+}-doped Zn–Al LDH materials can improve phosphate adsorption from water. The adsorption performance of Zn–Al LDH for phosphate was 43.83 mg g^{-1}. After doping with 1% Cu^{2+}, the adsorption capacity increased by 54.6% to 67.76 mg g^{-1}. The author attributes this performance to the Jahn–Teller effect of Cu^{2+}, which increases the hydrotalcite layer spacing and specific surface area. This is associated with facilitating the interlayer anion exchange. This doping distorts the hydrotalcite laminate, increasing the interlayer spacing, which in turn improves the adsorption of phosphate molecules.

Furthermore, Zn–Al and Mg–Al LDH materials were analyzed regarding the impact of phosphate adsorption.[51] The materials show rapid adsorption with an equilibrium time of 40 min. Zn–Al LDH shows higher phosphate adsorption than Mg-Al LDH. This behavior is associated with the higher specific surface area of ZnAl-LDH (135 m^2 g^{-1}) than MgAl-LDH (104 m^2 g^{-1}). The adsorption capacity decreased in basic environments (pH 8–12). The PSO model displays a proper fit for the kinetic data.

Freundlich and Langmuir's models were fitted for Mg–Al and Zn–Al LDH materials. The mechanism was proposed based on zeta potential determination and FTIR analyses. Phosphate adsorption is driven by LX, ES at the active sites, and ion exchange between the interlayer and phosphate species (Fig. 3).

Luengo et al.[52] reported the co-precipitation synthesis of Mg–Al layered double hydroxide (LDH) for phosphate removal. The material shows stability at a pH higher than 5, with an outstanding adsorption capacity of 2.25 mmol g^{-1}. The adsorption equilibrium was reached at 300 min. The analysis of the experimental data suggests that the mechanism may follow the AX, ES, and SC pathways.

Furthermore, LDH materials, which are based on Ca^{2+} ions, exhibit high performance in phosphate removal. Ca-Al LDH materials with different metal molar ratios and metal precursors were reported for phosphate remediation.[53] The obtained materials were CA-2, CA-3, and CA-4, according to the molar ratio of Ca and Al used from metal salts. The materials were labeled as CAs-2, CAs-3, and CAs-4, corresponding to metal molar ratios of 2 : 1, 3 : 1, and 4 : 1, respectively, based on the metal pieces. A preliminary experiment shows that the material's phosphate adsorption capacity increased with higher Ca content. The materials with the molar ratio 4 : 1 (CAs-4 and CA-4) display 120.83 and 125.00 mg g^{-1}, respectively. Based on this, the data
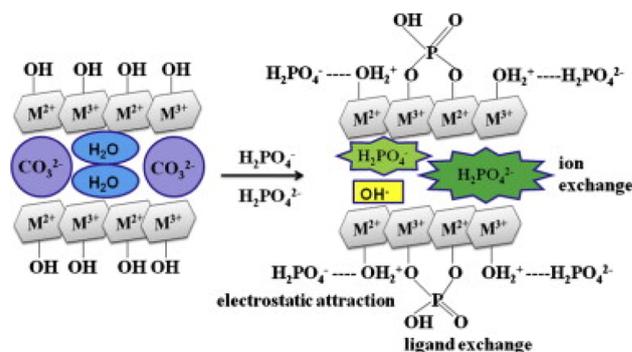

Fig. 3 Schematic diagram of possible adsorption mechanisms by LDHs. Reprinted from ref. 51 with permission from Elsevier, Copyright 2014.

were fitted to the Langmuir and the Freundlich models. The best fit with R^2 was 0.974 and 0.967 for Langmuir, indicating maximum adsorption capacities of 126.41 and 127.43 mg g^{-1}, respectively. Kinetic was governed by the PSO model, controlled by the chemical adsorption mechanism. The pH influence was tested in the range 2–12 for CAs-4 (Fig. 4a) and CA-4 (Fig. 4b). A decrease was observed in the pH range of 2–3 and 11–12, with the highest adsorption occurring at pH 7. The pH in equilibrium was higher than the original pH value because LDH is an alkaline material. Then, the phosphate speciation (Fig. 4c) and the zeta potential (Fig. 4d) in water must be considered. The isoelectric points of CAs-4 and CA-4 were 6.62 and 7.32, respectively. The surface changes positively at lower values, while at higher values, it is negative. This is in line with phosphate speciation and the low adsorption at acidic pH values, due to the ES repulsion of phosphate anions.

4.2 M^{2+}–Fe based LDH materials (M^{2+} = Zn, Mg)

As mentioned above, LDHs have been extensively studied as promising AX materials for phosphate capture from aqueous environments. Specifically, Fe-based LDHs have attracted substantial attention due to the strong affinity of the iron for phosphate.[93,94] This results in rapid and efficient phosphate adsorption, even at low concentrations. Moreover, Fe is an abundant, non-toxic element, thus offering low-cost, environmentally sustainable properties. Additionally, Fe-based LDHs incorporating Mg, Zn, and other metals have demonstrated synergistic properties, resulting in high phosphate capture, often with outstanding recyclability and stability across various pH conditions.[82]

A pioneering work utilising Fe to uptake phosphate was published in 2006 by Das et al.,[95] in which several different types of LDHs were synthesised by co-precipitation, including Mg–Fe and Zn–Fe. The samples were calcined, forming mixed-metal oxides that were used for phosphate adsorption. When the calcined materials were exposed to phosphate-containing solutions, the LDH structure was reconstructed, with phosphate intercalated in place of the original anions. The process could be performed across multiple cycles, but with reduced capacity after each cycle, highlighting a trade-off between adsorption efficiency and long-term reusability.

In 2008, Hongo et al.,[96] explored the adsorption properties and thermal behavior of Zn–Fe–based LDHs intercalated with sulfate ions, synthesized via co-precipitation. The experiments investigated the capacity to adsorb toxic anions, including arsenate, chromate, and phosphate. The results demonstrated a facile sulphate anion exchange for these compounds. Notably, the authors conducted detailed thermal analyses using TG–DTA and XRD to examine phase transitions upon heating. It was found that Zn–Fe LDH maintained structural integrity up to ∼200 °C but underwent significant decomposition at higher temperatures, transforming into mixed metal oxides. These thermal characteristics are crucial for rationalising the operability limits of the material in real-world applications, particularly in wastewater treatment systems where the temperatures tend to fluctuate.[97,98]

Liu et al.,[99] synthesized a nanocrystalline Zn–Fe LDH intercalated with chloride ions via a simple coprecipitation method, targeting enhanced phosphate adsorption. The material demonstrated excellent performance, with a high specific surface area (93.6 m^2 g^{-1}) and a maximum phosphate adsorption capacity of 89.2 mg g^{-1}, governed by SC and AX, as shown in Fig. 5. Spectroscopy characterisation suggested that phosphate adsorption involved substitution of interlayer Cl$^-$ and coordination with surface hydroxyl groups. While the LDH showed robust performance over a broad pH range (3–9), its regeneration ability declined significantly after three cycles, retaining only ∼80% of its original capacity due to structural degradation. Despite these results, it is essential to strike a balance between high capacity and recyclability, which is crucial for sustainable water treatment applications.
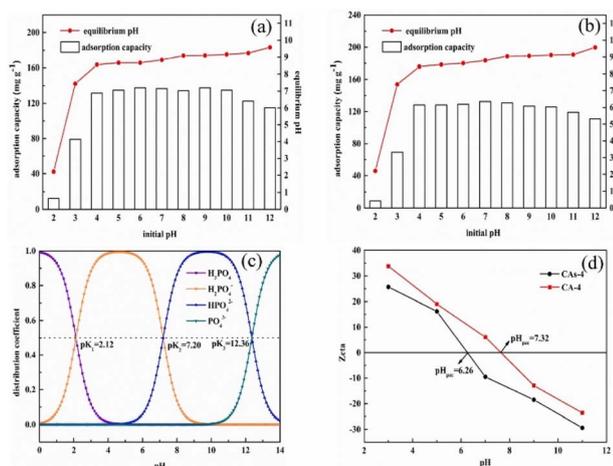

Fig. 4 (a) Effect of pH on CAs-4 adsorption of phosphate and final pH, (b) effect of pH on CA-4 adsorption of phosphate and final pH, (c) the phosphate speciation with varying pH value, (d) the zeta potential of CAs-4 and CA-4. Reprinted from ref. 53 with permission from Elsevier, Copyright 2022.
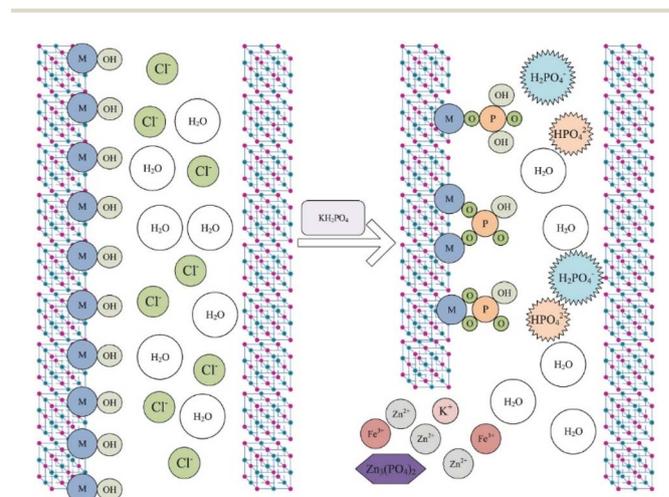

Fig. 5 Proposed mechanisms for phosphate in nanocrystalline Zn–Fe-based LDHs intercalated with chloride ions (M represents Fe or Zn). Reprinted from ref. 99 with permission from John Wiley & Sons, Copyright 2018.

Structural optimisation *via* metal selection is critical to LDH performance in phosphate capture. Zn–Fe LDHs, for instance, have demonstrated notable reactivity, as reported by Kim *et al.*,[100] where a combination of spectroscopic and computational tools enabled the elucidation of the roles of Zn and Fe in the adsorption process. These findings revealed that Zn can contribute significantly to phosphate uptake. At the same time, Fe remains structurally stable, supporting the synergistic effect of Zn-Fe in phosphate uptake and maintaining the structure after multiple use cycles.

Additionally, diverse bivalent and trivalent ions can be utilized for the synthesis of LDH. Zhang *et al.*[54] reported that an exploratory study was conducted using different M^{2+}/M^{3+} molar ratios to investigate the impact of phosphate adsorption. M^{2+} were Mg, Zn, and Fe, and M^{3+} were Al^{3+} and Fe^{3+}. In the initial screening test, a molar ratio of 2 was used. It was reported that using Al^{3+} centres exhibits higher adsorption than those using Fe^{3+}, indicating an effect of the trivalent ion. Mg-Al LDH displays higher phosphate removal amounts and faster kinetics than other LDHs. The Langmuir model reveals the maximum adsorption capacity of 76.1 mg g^{-1} under 25 °C. In this case, the ion size of Fe^{3+} is closer to Mg^{2+} compared with Al^{3+}, and the coordination environment of Al^{3+} is more similar to that of Mg^{2+}. As a result, the difference in adsorption performance of Mg–Al- and Mg–Fe-based LDH could be attributed to the stability of octahedral sheets influenced by the coordination preference. Also, it was reported that LDH with an interlayer anion of Cl^- had a slightly higher phosphate removal than LDH with an interlayer anion of NO_3^-. It was stated that the slight difference in adsorption performance was due to the subtle difference in the M^{2+}/M^{3+} molar ratio and the amount of anions in the formation of the layer structure.

4.3 M^{2+}-La based LDH materials (M^{2+} = Mg)

The incorporation of La in LDH materials has gained attention since it is an environmentally friendly rare earth element. La^{3+} is a strong Lewis acid with a high correlation with a strong Lewis base, as the phosphate molecule.[101] The use of novel techniques during synthesis can lead to improved adsorption efficiencies in LDHs.[102] Xu *et al.*,[103] reported a Mg–La LDH material with different Mg : La molar ratios (2 : 1, 3 : 1, and 4 : 1). The material with 4 : 1 ratios displays the best adsorption due to its faster kinetics. The maximum adsorption capacity is 87.23 mg g^{-1}. The adsorption mechanism was proposed as ES, IX, and SC.

4.4 LDH-based composite material

LDH-based composites have been reported to perform exceptionally for phosphate removal.[45] LDH exhibits an excellent phosphate ion removal capacity, derived from characteristics such as large surface area, thermal stability, and good AX capacity. However, their application in powder form is challenging. Therefore, several researchers have found that encapsulating LDH in different polymers facilitates easier separation and prevents LDH agglomeration during removal.[104–106] Chitosan is one of the most commonly used polymers in composites, ranking as the second-longest polysaccharide in the world and

being extremely useful for encapsulation due to the amino, hydroxyl, and carboxyl groups it possesses.[107] Given the above, numerous studies have been conducted on phosphate removal using chitosan composites. An example is the LDH hydrogel beads with embedded chitosan.[70] The rare earth-based layered double hydroxide/chitosan hydrogel beads, LaCa-LDH/CS and CeCa-LDH/CS, displayed up to almost double the maximum adsorption capacity of LDHs on their own, demonstrating remarkable performance in the range of 3–7 for CeCa-LDH/CS, and in 3–11 pH for LaCa-LDH/CS. In addition to the above, the exceptionally long-term adsorption stability test (10 days) demonstrated the substantial real-world capability of both adsorbents. In parallel, polyvinyl alcohol/metal ions sodium alginate (PS-M-LDH, M = Ca^{2+}, Fe^{3+}, Al^{3+}, La^{3+}) beads synthesized through *in situ* crosslinking revealed that PS-La-LDH exhibits the highest phosphate removal capacity, 91.2 mg P g^{-1} LDH, which is 1.6 times higher than that of pristine LDHs. Based on SEM-EDS, FTIR, XRD, and XPS, the phosphate interaction mechanisms were driven by protonation, ES, LX, and IX (Fig. 6).[45]

Due to its mechanical strength, high stability, and flexibility, poly(vinylidene fluoride) (PVDF) is useful for encapsulating adsorbents. However, the PVDF's hydrophobicity presented a challenge for its application in water remediation. As a result, Kim *et al.*,[78] implemented poly(vinyl alcohol) (PVA) to increase hydrophilicity due to its miscibility with PVDF in LDH-embedded beads for phosphate removal. The synthesized Mg-Fe LDH beads demonstrated that incorporating PVDF and PVA improves recyclability and stability. Moreover, Kumar and Viswanathan[60] evaluated the application of magnetic-chitosan-assisted hydrotalcite (MCSHT) and magnetic-alginate-assisted hydrotalcite (MAlgHT) in phosphate removal. Both composites showed improved removal of the components individually, due to the presence of –OH groups and Fe^{3+} ions. However, the MCSHT showed higher adsorption capacity than MAlgHT,
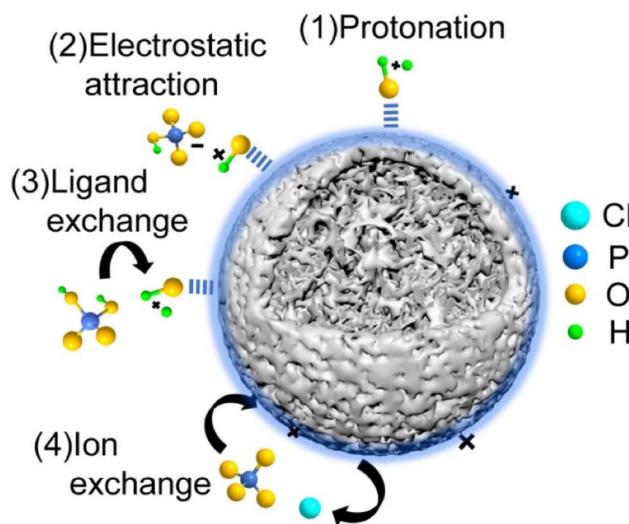

Fig. 6 Schematic diagram of the possible phosphate adsorption mechanism of PS-La-LDH. Reprinted from ref. 45 with permission from Elsevier, Copyright 2022.

attributed to the $-NH_2$ groups contained in chitosan. The proposed removal mechanism for both composites includes SC, ES, and IX (Fig. 7).

Alternatively, the composite resulting from the cross-linking of MgFe-LDH immobilization in polymer, hybrid gel microspheres, efficiently removed phosphorus from eutrophicated water.[108] An improved performance was observed at higher pH levels, due to the transformation from P-insoluble to P-soluble, which was promoted by the composite. Phosphorus analysis of the sediments showed the presence of 5 phosphorus species, including NaOH-P (Fe/Al-P), HCl-P (Ca-P), OP (organic P), IP (inorganic P), and TP. At pH 8, the saturation capacity of the MgFe-LDHs hybrid gel microspheres was achieved for IP (1020 mg kg^{-1}), OP (392 mg kg^{-1}), NaOH-P (745 mg kg^{-1}), and HCl-P (196 mg kg^{-1}). The LX and complexation between MgFe-LDHs and IP were suggested as possible determinants of phosphorus adsorption by MgFe-LDH hybrid gel microspheres. Recently, Li et al.,[109] reported a study in which a sustainable synthesis of LDH materials was achieved. The authors synthesised Mg-Fe/Al LDHs from red mud and sludge, producing granular materials suitable for column filtration systems. Utilising these reagents as raw materials is a further step towards generating more sustainable materials in water purification. This work underlines the sustainability advantage of Fe-based LDHs when sourced from industrial by-products.

Due to their easy separation process, LDH-magnetic-based materials have been reported for the removal of phosphates.[56] Alagha et al.[57] reported a composite based on Mg–Fe LDH with sludge-based activated carbon (SBAC-MgFe) for phosphate removal, with an eco-friendly approach (Fig. 8). The kinetic data were best described by the pseudo-first-order (PFO) model, suggesting a physical process driven by ES and IX. According to the Langmuir model, the maximum adsorption capacity was 109.9 mg g^{-1} at 318 K and pH 3. The adsorption mechanism was proposed as HB and $\pi-\pi$ interactions.

Conversely, the prepared $Fe_3O_4@mSiO_2@mLDH350$ composite,[62] featuring MgAl-LDH and Fe_3O_4 microspheres as
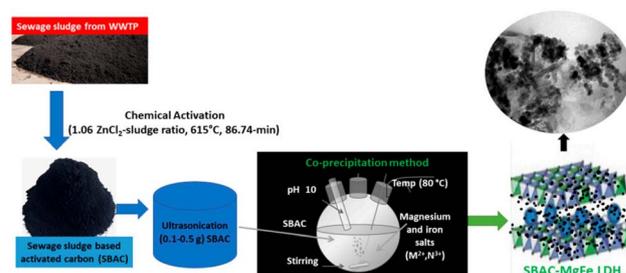

Fig. 8 Schematic diagram of the synthesis of magnetic Mg–Fe/LDH composite intercalated with sludge-based activated carbon (reprinted with permission from ref. 57 copyright 2020 MDPI, Basel, Switzerland, under the terms and conditions of the Creative Commons Attribution (CC BY) license).

the core and a SiO_2 matrix as the inner layer, demonstrated maximum Langmuir adsorption capacities for phosphate and fluoride of 57 and 28 mg g^{-1}, respectively, in removing phosphate and fluoride from water. pH influence studies showed superior phosphate adsorption over fluoride. $Fe_3O_4@mSiO_2@$-mLDH350 exhibited over 90% removal at initial phosphate concentrations of 2 to 30 mg L^{-1} and pH 3 to 12, with minimal variation in removal.

Similarly, the magnetic Fe_3O_4/Zn-Al-Fe-La layered double hydroxides (LDHs) reported by Qiao et al.,[80] reported that since lanthanum has a high affinity for anionic contaminants, it is that, along with the incorporation of magnetic Fe_3O_4, the quaternary metal Fe_3O_4/Zn-Al-Fe-La-LDH composite removes and recovers phosphate from simulated sewage. Additionally, since water eutrophication frequently co-exists with anions, the composite was evaluated in the presence of chloride, sulphate, carbonate, fluoride, and nitrate. The adsorption capacity decreased slightly in the presence of Cl^- and F^-. However, in the presence of CO_3^{2-}, it was dramatically reduced due to increased competition with phosphate anions.

Li et al.[65] synthesised the MgFe-LDH with magnetic bi-ocarbon from renewable agricultural residues, labelled as MBC@LDH. Using mulberry branches, they prepared a biochar that enhanced phosphate removal when combined with the AX capacity of LDH, capitalizing on the biochar's porosity. The performance evaluation of MBC@LDH for phosphate adsorption demonstrated a removal rate of over 85% in the pH range of 4–9. In addition, it exhibited excellent selectivity towards Cl^- and NO_3^- ions, with a removal rate of >87% after three adsorption–desorption cycles. The contribution of magnetic particles in the MBC@LDH reduced the separation time by 72% compared to the centrifugation method. On the other hand, $MnFe_2O_4$/ZnFe-LDH synthesised by co-precipitation demonstrated that the incorporation of $MnFe_2O_4$ not only allowed for easier separation, but also improved phosphate removal (94.52 mg g^{-1}) and chromium(VI) (49.03 mg g^{-1}) removal above that obtained for ZnFe-LDH.[74] The pH study showed an increase in efficiency in the 2–5 pH range due to positive charge density on the surface and the presence of $H_2PO_4^-$ in acidic conditions, which favours phosphate removal. Conversely, under alkaline
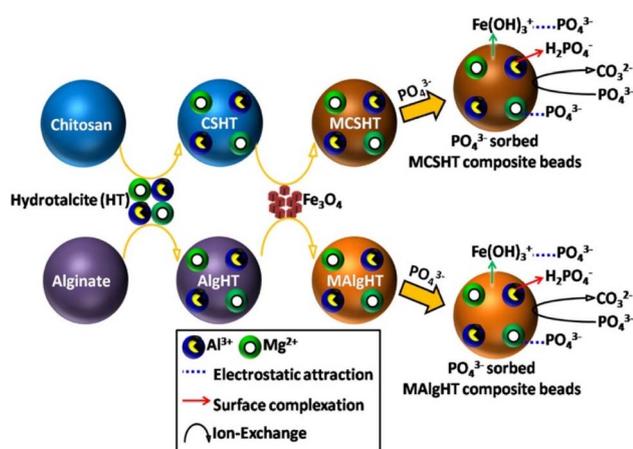

Fig. 7 Phosphate removal mechanism by MCSHT and MAlgHT composite beads. Reprinted from ref. 60 with permission from American Chemical Society, Copyright 2019.

conditions, the competition between the –OH and HPO_4^{2-} and PO_4^{3-} groups for interaction sites increases.

Similarly, Koilraj et al.,[76] using a molar ratio of Mg/Al of 2, synthesised Mg_2Al-NO_3-LDH, which incorporated Fe_3O_4 to produce Fe_3O_4/Mg_2Al-NO_3-LDH, demonstrating that it achieved a higher adsorption capacity than Fe_3O_4. PXRD characterisation demonstrated anion exchange between the phosphate in the solution and the nitrate contained in the LDH interlayer space. Furthermore, in dependence on the phosphate concentration, they describe the adsorption in three steps. At low concentration (0.25 mM), the interlaminar distance collapses due to the high valence of the phosphate anions, which exchange nitrate anions, resulting in a decrease in the interlaminar space. Then, at intermediate phosphate concentrations (0.5 to 1.125 mM), the phosphate ions' larger ionic radius in the interlaminar space increases the interlaminar distance. And, at high concentrations (>1.25 mM), the interlaminar distance is reduced due to electrostatic interactions between the positively charged host layer and phosphate anions. Then, Fe_3O_4/Mg_2Al-NO_3-LDH was compared in terms of performance in enriched sea and deionised water under optimised conditions (1.0 g L^{-1} sorbent amount) for 6 h at 100 rpm agitation at pH 8.2. The results showed that 100% phosphate sorption occurred in deionised water. However, seawater enriched with phosphate showed a sorption capacity of 58%, and the adsorption increased to 86% when the sorbent concentration was increased to 3.0 g L^{-1}. This reduction in removal efficiency is due to the presence of co-existing anions, such as chloride and sulphate, which increase ionic strength. Therefore, Fe_3O_4/Mg_2Al-NO_3-LDH can be utilised for treating natural water streams.

Sheng et al.,[110] compared magnetic Mg–Al-, Zn–Al-, and Mg–Fe-based LDHs for phosphorus adsorption, demonstrating that Zn–Al had the highest adsorption capacity (80.8 mg g^{-1}), followed by Mg–Al (74.8 mg g^{-1}) and Mg–Fe (67.8 mg g^{-1}), with adsorption driven by ligand exchange and hydroxyl–phosphate interactions. However, it was also noted that coexisting anions, such as bicarbonate, could significantly inhibit performance, and stability issues limited practical application. By reducing the particle size of the Fe_3O_4, superparamagnetic composites can be formed. Sürmeli et al.,[111] investigated this superparamagnetic nanocomposite microparticles modified with different Fe-based LDHs for phosphorus removal. The non-optimised samples were unstable under acidic conditions. At the same time, the optimised composition, containing 500 mg of nanocomposite microparticles (NCMP) and 60% LDH, achieved a phosphorus removal efficiency of 18.5% and a specific removal capacity of 53.1 mg g^{-1}. Furthermore, the modified Fe-based LDHs exhibited excellent magnetic separability (96.9%).

Due to their improved physicochemical properties, such as tunable functionalization and enhanced surface area, carbon-based composites have attracted significant attention.[112] Moreover, several low-cost methods for preparing carbon-based composites, such as utilising biomass, have been reported, enabling simple, environmentally friendly approaches.[113] The low-cost adsorbent composite BBAC@Zn–Al ()LDHs, synthesised by co-precipitation (Zn–Al LDHs wrapped into activated carbon), was reported to exhibit good recyclability up to

five cycles.[73] Banana Bract was selected as a carbon source for the synthesis due to its high surface area and the presence of various reactive groups, including hydroxyl, carbonyl, phenolic, and carboxylic groups. However, it was found to be inactive after the seventh cycle due to the opposing OH^- ions from the NaOH solution, which occupied the active sites, where NaOH was the desorbing agent. Through FTIR and EDAX analysis, it was found that the presence of M–OH groups was related to inner-sphere and outer-sphere complexation. Furthermore, through IX, the surface hydroxyl groups of the LDH are exchanged for phosphate. Additionally, ES reactions occur between the positively charged surface and the PO_4^{3-} anions.

The conditions and synthesis process, such as uncontrolled sheet stacking, can affect properties such as surface area and the number of active sites.[114] Thus, in an effort to improve the performance of LDH-BC composites, Li et al.,[64] evaluated the 'support effect'. The results showed that the prepared LDHs on ball-milled biochar (LDH-BMBC) exhibited smaller particle and crystallite sizes, improved surface area and porosity, as well as the addition of O-containing functional groups. These enhancements were reflected in an improvement in phosphate removal performance. LDH-BMBC doubled the adsorption of LDH-BC. Furthermore, they reported that the phosphate was adsorbed on the interlaminar spacing, as indicated by the XRD results, which showed an increase in the interlaminar spacing after adsorption. This phenomenon is a characteristic manifestation of the anion exchange mechanism, where the initial, smaller interlayer anions are replaced by the larger phosphate species, resulting in the structural expansion of the layered lattice. Along with XPS and FTIR analysis, suggested that adsorption occurs through the contribution of five possible interactions, including physical adsorption, AX, ES adsorption, monodentate, and bidentate coordination (Fig. 9).

In addition to the synergetic effects of LDH composites on phosphate removal, zirconium-modified LDH can enhance LDH performance as reported by Motandi et al.[66] They evaluated the modification of the commercial MgAl-LDH, yielding Zr-LDH, and its 500 °C calcined analogue, Zr-LDO, on phosphate adsorption from water. SEM-EDS showed a homogeneous distribution of Zr on the surface of Zr-LDH and Zr-LDO, while by XRD, the Zr-LDH
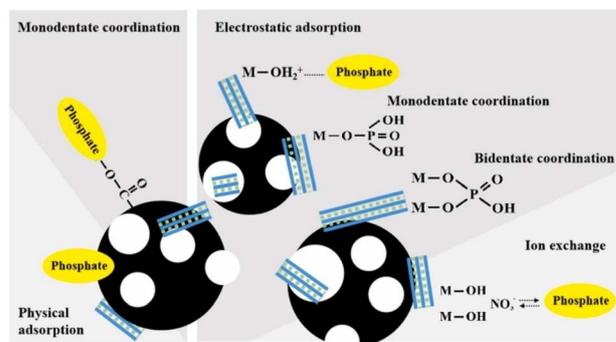

Fig. 9 Schematic illustration of possible mechanisms for phosphate adsorption on LDH-BMBC. Reprinted from ref. 64 with permission from Elsevier, Copyright 2022.

showed high crystallinity and a hexagonal crystal structure. Conversely, Zr-LDO showed the Zr-containing conversion in the Zr-LDH to zirconium oxides, and a decrease in crystallinity. Contact time analysis revealed rapid adsorption, reaching equilibrium at 70 min for Zr-LDH (98%), Zr-LDO (95%), and LDH (67%). A fit to the pseudo-second-order model yielded a regression coefficient of 0.999 for all three adsorbents. The Langmuir isotherm fit showed a maximum adsorption capacity of 90, 80, and 69 mg g^{-1} at 298 K for Zr-LDH, Zr-LDO, and LDH, respectively. Similarly, Nuryadin et al.,[79] analysed the influence of the Zr/Fe molar ratio (0.5–2) on the synthesised Am-ZrO$_2$/MgFe-LDH composites. The evaluation of phosphate adsorption revealed that the composite with the highest amorphous ZrO$_2$ content exhibited the highest adsorption capacity. The authors also evaluated the same composites in their calcined form. Calcination reduced adsorption capacity by eliminating hydroxyl groups. Additionally, the composite exhibited maximum desorption capacity (87.37%) at 40 min using a 2 N NaOH solution; however, the difference using 1 N NaOH was negligible (Fig. 10a). Based on the above, the percentage yield decreased with each adsorption–desorption cycle, from 95% to 78% in the seventh cycle (Fig. 10b).

Cheng et al.,[77] evaluated a novel Al-doped iron oxide-decorated layered double hydroxide nanocomposite (Al-Fe$_2$O$_3$/LDH) for the removal of phosphate and organic dyes from water. By synthesis via a one-step hydrothermal method, it is

proposed that the presence of layered hydroxide nanoflakes can modulate the growth of oxide nanoparticles. This was achieved by adding different concentrations of iron (Fe(NO$_3$)$_3$·9H$_2$O) to the synthesis solution. They found that Al-Fe$_2$O$_3$/LDH with 1.0 mmol of iron had the highest phosphate adsorption capacity. However, as the iron content increased, the adsorption capacity decreased. The integration of Al-Fe$_2$O$_3$ and the inhibition of LDH nanoflake growth contributed to the addition of excess iron contents, leading to a heterogeneous surface with different types of adsorption sites. The evaluation results demonstrated that the synergistic effect of LDH nanoflakes and supported Al-doped iron oxides promoted exceptional adsorption kinetics and a high adsorption capacity, with adsorption primarily occurring within the first minute, yielding a capacity of 93.06 mg g^{-1}.

A significant drawback of adsorption is its low effectiveness at low concentrations. Composites, such as activated carbon, have been introduced to address this issue.[115] The LDHBC composite, which evaluates the synergistic effects of Fe-Mg/LDH and Douglas fir biochar, demonstrated a six-fold increase in the adsorption capacity of LDH.[58] In addition to exceptional performance in the pH range of 1–11, it demonstrated selectivity in the presence of nine other anions (CO$_3$$^{2-}$, AsO$_4$$^{3-}$, SeO$_4$$^{2-}$, NO$_3$$^{-}$, Cr$_2O_7$$^{2-}$, Cl^{-}, F^{-}, SO$_4$$^{2-}$, and MoO$_4$$^{2-}$) and effective removal at low concentrations. The mechanism proposed for low concentrations (10–500 mg L^{-1}) was IX, whereas for high concentrations (>500 mg L^{-1}), it was chemisorption and the formation of stoichiometric phosphate compounds. Phosphate adsorption was verified using various techniques, including SEM (Fig. 11).

Similarly, the La-MgFe-LDH/BC composite, synthesised by Shan et al.,[63] through co-precipitation, demonstrated that the implementation of lanthanum (La) improved the LDH properties, resulting in smaller particle sizes, improved porosity, and an enrichment of carbonate groups. This incorporation showed a decrease in Fe as a function of La enrichment. These improvements offered effective removal, reaching concentrations of 0.01 mg(P) L^{-1} of phosphate from real secondary effluents and raw sewage, as well as exceptional reusability with over 90% desorption efficiency. Through density functional
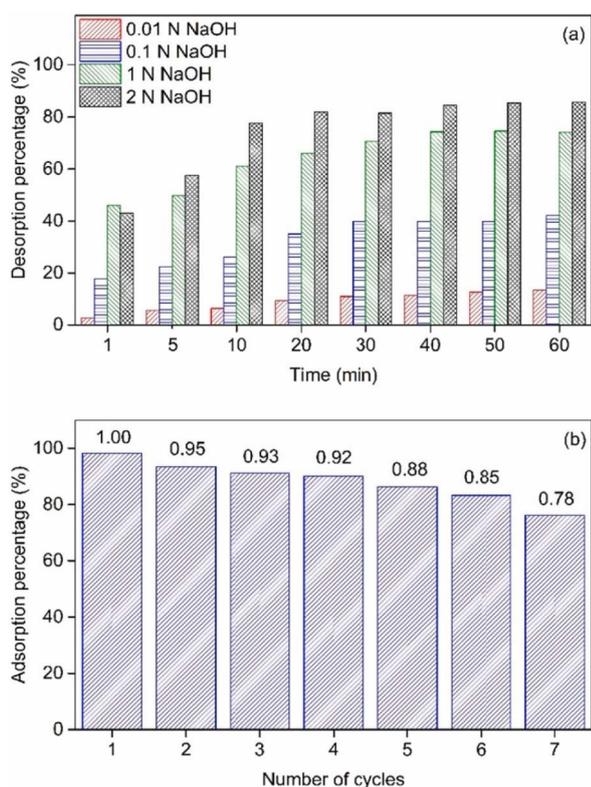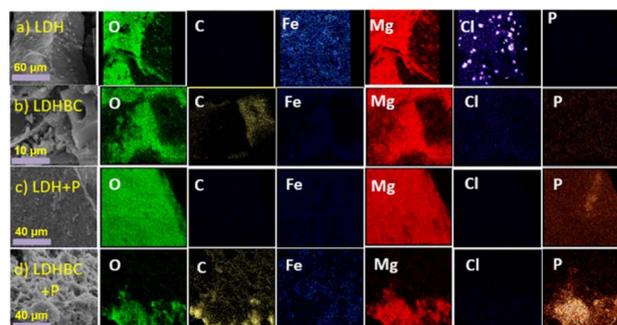

Fig. 10 (a) Phosphate desorption by different concentrations of NaOH solution, and (b) the reusability of composite for phosphate adsorption with desorption solution of 1 N of NaOH (the numbers above the bar are adsorption retain ratio of phosphate adsorption by the composite). Reprinted from ref. 79 with permission from Elsevier, Copyright 2021.

Fig. 11 SEM/EDS elemental maps for (a) LDH, (b) LDHBC, (c) phosphate-laden LDH (234.3 mg g^{-1} phosphate), and (d) phosphate-laden (1279.6 mg g^{-1}) LDHBC. Reprinted from ref. 58 with permission from Elsevier, Copyright 2021.

theory and characterization (Fig. 12a), the interaction mechanism was analyzed. It was described as a contribution of ES, AX, inner-sphere complexation, and SP, with La incorporation facilitating electron transfer and lowering adsorption energies (Fig. 12b).

On the other hand, the implementation of membrane technology, such as that synthesised by Fang et al.,[116] contributes to the removal of phosphate from water. The membrane successfully removed phosphate without the assistance of flocculation. Furthermore, derived from the active sites embedded in LDH, it achieved an outstanding phosphate retention capacity, reducing its concentration to a mere 0.05 mg L^{-1} with a load of 1146.5 mg m^{-2} h^{-1}, enabling the processing of up to 4400 bed volumes of wastewater, and reaching concentrations of 0.1 mg L^{-1}. The membrane production employed an MgAl-LDH synthesized by co-precipitation. By vacuum filtration, a suspension of LDH was filtered onto the 0.45 μm membrane, 47 mm in diameter, supported on the surface (Fig. 13a). Phosphate adsorption was through a filter pre-loaded with the synthesized membrane (Fig. 13b). The performance in real wastewater, with 0.92 mg L^{-1} of phosphate, in the presence of coexisting SO_4^{2-}, NO_3^-, and Cl^- ions, proved to be efficient in alleviating the

problem of rapid growth of transmembrane pressure due to floc accumulation and reducing the frequency of backwashing.

The Go/MgMn-LDH-300 composite, synthesised by Lai et al.,[71] offers exceptional recyclability and selectivity, and it also performs phosphate adsorption–desorption through innovative electro-assisted technology. Through a continuous electro-assistance method, the electrostatic interactions were controlled by varying the potential difference, resulting in desorption and, consequently, effective recyclability. Characterisation of the GO/MgMn-LDH-300 composite revealed that the integration of graphene oxide (GO) improved mesoporosity, and the contribution of oxygen-containing functional groups in GO favoured the presence of more phosphate-specific active sites. The above approach demonstrates that the use of methods/techniques complementing adsorption is a valuable tool for improving adsorbents to overcome eutrophication.

Similarly, the environmentally friendly NiFe-LDH/rGO electrically switched ion-selective (ESIX) film system, synthesised by Ma et al.,[75] besides showing excellent cyclic stability, performs desorption through the controlled ion exchange system. Unlike traditional electrochemical techniques such as capacitance deionisation, ESIX offers greater adsorption and desorption selectivity (Fig. 14a) due to the deposition of LDH in the conductive matrix, while controlling the redox potential through a potential regulation method. Furthermore, this method does not involve chemical agents, avoids secondary pollution, and is suitable for removing low concentrations of contaminants. The NiFe-LDH/rGO hybrid film has certain adsorption performance for PO_4^{3-}, SO_4^{2-}, NO_3^- and Cl^-, its adsorption performance for phosphate anions is significantly superior to other anions (Fig. 14b). This system demonstrated improved dispersion of LDH sheets, enhancing phosphate adsorption and achieving an outstanding adsorption capacity of 270 mg g^{-1}.

Often, doubts arise regarding the disposal of the adsorbent after it has completed its function. Based on this, the colloidal suspension of Ni-Al/LDH, synthesized by hexamine hydrolysis,
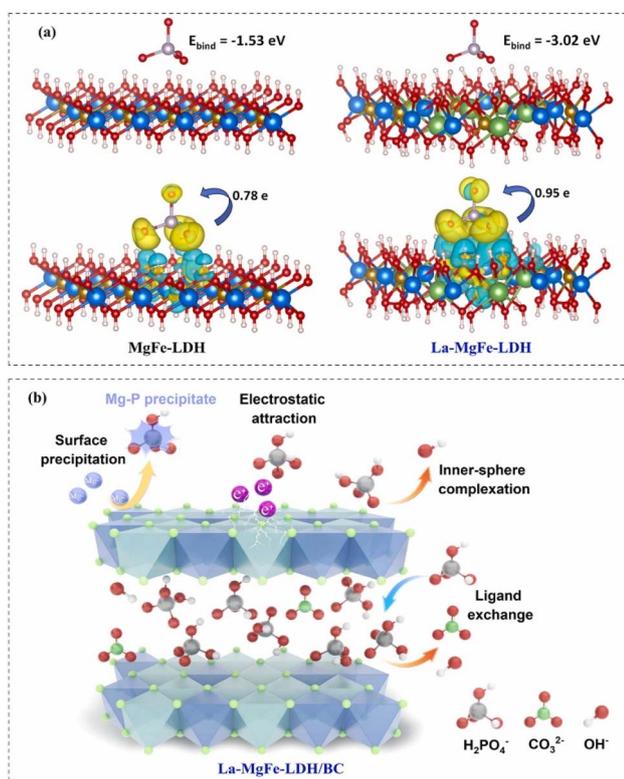

Fig. 12 (a) Schematic comparison of adsorption energy and differential charge density distribution for phosphate sorption on (003) planes of MgFe-LDH and La-MgFe-LDH, with atom colors blue, brown, green, red, purple, and grey representing Mg, Fe, La, O, P, and H, respectively; the yellow and cyan areas indicate charge accumulation and depletion, respectively. (b) Proposed phosphate sorption mechanisms for La-MgFe-LDH. Reprinted from ref. 63 with permission from Elsevier, Copyright 2025.
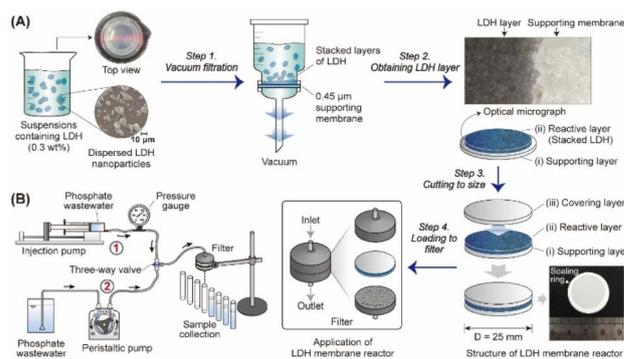
Fig. 13 Preparation and application of LDH membranes. (A) Is the schematic diagram of the steps to prepare LDH membranes by vacuum filtration. (B) Displays two positive pressure filtration systems for testing LDH membranes. The injection pump system was used to monitor transmembrane pressure and the peristaltic pump system was employed to study the phosphate retention performance. Reprinted from ref. 116 with permission from Elsevier, Copyright 2023.
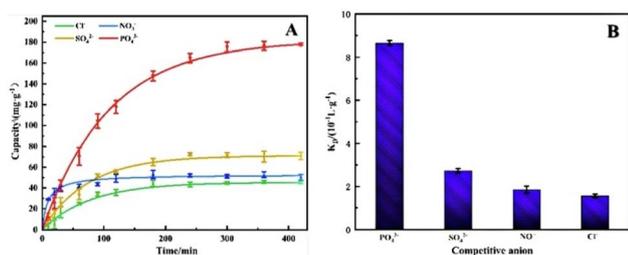
Fig. 14 (A) Competitive adsorption curve and (B) separation coefficient of PO_4^{3-}, SO_4^{2-}, NO_3^- and Cl^- for NiFe-LDH/rGO hybrid films at an initial concentration of 300 ppm. Reprinted from ref. 75 with permission from Elsevier, Copyright 2022.

was studied to determine the effect of the degree of dispersion by ultrasonication (UD-LDH), mechanical shaking (SD-LDH), and hydrothermal (HD-LDH) methods, and the restacked material after phosphate removal was utilized as an effective phosphate release fertilizer for the growth of a common green seaweed, Ulva lactuca.[59] The UD-LDH suspension reached the highest dispersion degree of 6.15 g L^{-1}. The 44–48 mV zeta potential values, along with the six-month evaluation, where the suspension was not settled, inferred the high stability dispersion. In laboratory experiments, UD-LDH and its analogue, the dried parent sample (NO_3-Hex-LDH), achieved a removal rate of above 97%. However, in the simulated model pond study without mechanical agitation, the UD-LDH suspension exhibited rapid adsorption rates, which were higher than those of NO_3-Hex-LDH, attributed to the suspension facilitating contact with the phosphate anion. On the contrary, NO_3-Hex-LDH settled to the bottom, hindering the contact with phosphate anions. Furthermore, in an attempt to recycle the waste derived from the phosphate ion removal, phosphate-loaded UD-LDH (UD-phosphate-LDH) was employed as a fertilizer, as a phosphate supplier, for the growth of the common green seaweed U. Lactuca (Fig. 15), displaying the blank control (Fig. 15A), UD-phosphate-LDH (Fig. 15B), CO_3-coppt-LDH (Fig. 15C), and NO_3-Hex-LDH (Fig. 15D) in 30 PSU seawater. The UD-phosphate-LDH growth results of 27% were compared with the control experiments (on Provasoli enriched seawater medium controlled with glycerol phosphate) of 29%, CO_3-
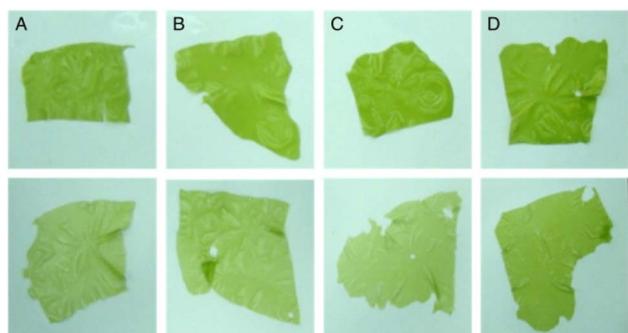
coppt-LDH, carbonate containing NiAl LDHs with Ni/Al atomic ratio around 2.0, of 25%, and NO_3-Hex-LDH of 23%.

5. Real wastewater application of LDH materials

Stability of LDH systems is necessary for an effective treatment of P-containing wastewater. An unstable material can lead to reduced reusability and increased pollution due to the leaching of metal ions and interlayer anions. Several factors contribute to the fragility of LDH, including the pH, metal, and inorganic ions present in the medium. Specifically, carbonates, sulphates, and phosphates can replace the pre-existing interlayer anion in the material through a competitive anionic exchange process. This results in damage to the material's architecture and, consequently, its stability. All these issues have made the real application of these materials barely explored. They are an interesting opportunity for the community to examine these systems in search of a stable potential application.[117–119]

Recently, Sonoda and coworkers identified a stable form of LDH, MgFeZr-CO_3-LDH, which demonstrated remarkable stability, maintaining over 92% adsorption/desorption capacity after ten cycles. The results illustrated the efficiency of the material in treating phosphorus-laden wastewater.[67] A similar LDH stable material was reported by Cao et al., who found that a mere 0.02 g L^{-1} of CaLa-CO_3-LDH reduced the phosphate concentration from 0.58 to 0.03 mg L^{-1} within 30 minutes (wastewater from a plant in Guangzhou, China). Another promising approach involved the biochar–MgAl–LDH composite reported by Alagha et al., which achieved an 84.80% removal rate from wastewater with an initial phosphate concentration of 3.68 mg L^{-1}. This excellent performance was attributed to the synergetic influence of the MgAl–LDH incorporated into the biochar.[68]

A pioneering synthesis was reported by Hu et al., in which BR-LDH was prepared under alkaline conditions using industrial residues, including boron mud and red mud, demonstrating an outstanding phosphate removal rate of 96.81% in wastewater from Beijing.[69] As mentioned before, MgLa-LDH was reported for phosphate adsorption by controlling the abundance of oxygen defects by varying the preparation pH, which led to improved phosphate adsorption efficiency.[61] The material was used for a real wastewater continuous flow column, which demonstrated similar results to those obtained in the batch experiment. The results highlight this methodology to synthesize materials, which offers a promising avenue for enhancing materials for efficient phosphate removal. Despite these promising results, it is clear that further investigation is necessary to take the next step in applying these materials in an industrial setting.

6. Outlook and future directions of LDH

The evolution of LDHs from a "promising material" to functional infrastructure for phosphorus capture and circular valorization necessitates the integration of material ecodesign,

Fig. 15 Photographs of seaweed U. lactuca before (top) and after (bottom) growth using (A) blank (control), (B) UD-phosphate-LDH, (c) CO_3-coppt-LDH, and (d) NO_3-Hex-LDH in 30 PSU seawater. Reprinted from ref. 59 with permission from Elsevier, Copyright 2013.

verifiable operational and regeneration parameters, pilot/demonstration-scale validation, and regulatory governance into a cohesive techno-operational framework, all grounded in comparable life-cycle and cost-benefit metrics (*e.g.*, $ per kg-phosphate removed; $ per m^3 treated). This systemic approach is not solely programmatic; it is based on documented process-control and scale-up frameworks.[120] It can be illustrated by synthesis and scaling,[121] and implemented through economic indicators.[122,123]

Expanding on that framework, safety and "by-design" toxicology transition from a secondary consideration to a fundamental design criterion: the integration of XRD/FT-IR/SEM/BET with DLS/ζ, multitrophic bioassays, and cellular MTT/MTS facilitates the translation from model media to practical conditions, while distinguishing shading/heteroaggregation and oxidative stress as predominant mechanisms in aquatic organisms, as demonstrated in the LDH toxicity studies referenced in the source material. At the cellular level, adjusting size and charge, applying surface coatings, and using endocytic pathways facilitate safety-by-design *via* intercalation and functionalization.[124]

This framework aligns with risk assessments and directives for lamellar materials, clarifying the regulatory trajectory,[125,126] ensuring that synthesis decisions and media formats are inherently compliant and traceable. In accordance with the aforementioned, phase stability and media format must be determined by the desired application. Immobilization in biopolymers—such as LDH/chitosan beads infused with La or Ce—maintains efficacy at pH 3–7, endures competing anions, and retains over 95% effectiveness after at least five cycles with 0.1 M NaOH; additionally, biochar-supported LDH facilitates the "functional" stabilization of phosphorus towards pyro/hydroxyapatite, beneficial for gradual release in soils, albeit with a reduction in crystallinity. Consequently, the choice map delineates granulars/hydrogels for stable aqueous polishing and LDH-biochar when fertirecycling is essential.[70,127]

The chosen format is contingent upon several factors, including its impact on regeneration, energy consumption, and end-of-life issues. Regeneration, intrinsically linked to format, refers to the execution of an action that is economically and structurally rational. A concentration of approximately 1.0 M NaOH for 20 to 60 minutes is optimal for desorption, accelerating the attainment of equilibrium. More of it doesn't help and makes leaching more likely. For sensitive composites, 1 M NaHCO$_3$ is a better choice. When heat activation is controlled, the memory effect (LDO → LDH) in LDO-based adsorbents allows sites to become available again. The results are substantiated by multicriteria verification (XRD/SEM/EDS/ICP-OES; mass loss) in magnetic particles and membranes.[116,128,129]

Therefore, to prevent "false positives" based only on transient efficiency, the referenced studies suggest categorizing a medium as "regenerated" only when crystalline/morphological consistency is maintained, mass loss is below the threshold, and performance is steady after ≥10–20 cycles. With media and regeneration delineated, process designs demonstrating optimal readiness combine seamlessly: stirred reactor combined with High-Gradient Magnetic Filtration using LDH magnets (about 1 hour contact at pH approximately 4.5, ~0.25 T separation, regeneration with 1 M NaOH and 1 M NaCl) and packed beds with an empty bed contact time of approximately 30 minutes in high-salinity/sulfate matrices. Both pathways demonstrate adequate capacity (tens of mg g^{-1}) in actual water samples, connecting laboratory and pilot studies.[46,120,130]

Simultaneously, material supply can be maintained through continuous hydrothermal synthesis (CHS) and the epoxide route (RT/1 atm) without compromising BET or crystallinity, as demonstrated by Seijas-Da Silva *et al.*,[121] and examined by Clark *et al.*;[120] that is, process scale and synthesis scale progress concurrently. This link directly influences sustainability and life cycle assessment (LCA): convergent evaluations highlight NaOH consumption and regeneration/wash energy as critical hotspots; hence, studies advocate for recovering at least 90% of wash water, documenting the number of washes, and considering the site's energy mix. Comparative analysis elucidates trade-offs: Ca-LDH can exceed 190 mg g^{-1}, leading to irreversible transformations (apatite), while LDH–biochar promotes regenerability and controlled release in soil, necessitating monitoring of metal accumulation with repeated applications.[82,117,131–133]

Consequently, media and process selections conclude with an analysis of life cycle and cumulative risk. Modifications and nanocomposites in solid-state design serve as precise mechanisms for connecting performance, altering M^{2+}/M^{3+}, the interlayer anion, and exfoliation/delamination or integration with carbons/polymers, thereby enhancing basic-site density and interlayer diffusion of PO_4^{3-}. Hierarchical Fe$_3$O$_4$@SiO$_2$-|LDH(MgFe : Zr) architectures effectively enhance magnetic separability, structural integrity, and anion affinity, achieving approximately 96% removal and 85% recovery within 60 minutes using 1 M NaOH under verifiable regeneration protocols.[134–136] Material and process are interconnected *via* separability and cycle stability. The identical rationale of integration applies to standardization and regulatory compliance: if the objective is green-by-design and a circular economy, synthesis pathways must minimize energy and effluents, utilize circular inputs (*e.g.*, struvite/fly ash) to close loops, guarantee functionalization traceability, and undergo standardized stress tests (pH, Cl$^-$/SO$_4^{2-}$, column operation) with comparable key performance indicators (KPIs). This framework, analyzed by Rybka & Matusik,[137] and Chen *et al.*,[138] is methodologically supported by precedents for lamellar materials.[125,126]

Synthesis innovation ultimately serves as the mechanism that completes the design–process–regeneration cycle: the epoxide method (RT/1 atm) with *in situ* monitoring (SAXS/XANES), interfacial dissolution–reprecipitation (IDR) in a closed loop (approximately 20 wt%; NaOH recycling, meixnerite product suitable for anion exchange), and CHS with increased flow rates without compromising BET/crystallinity establish a production framework; concurrently, reducing carbonation (approximately 7.3% CO$_3^{2-}$) during fabrication and handling maintains OH$^-$ sites and exchange kinetics.[120,121,139] In this framework, unit economics are not a conclusion but essential to technology selection: capacity in

actual matrices under ionic competition must be paired with \$ per kg-phosphate and \$ per m³, detailing NaOH/NaHCO₃ consumption per cycle, adsorbent mass loss, and wash-water recovery of at least 90%. Within the parameters of feasible operation—23–35 mg g⁻¹ in slurry-HGMF (pH approximately 4.5–5, 45–60 minutes)—these indicators facilitate technology comparisons and assess sensitivity to energy and washing.[122,123,132,137]

In sum, the connection among material, process, regeneration, sustainability, and compliance delineates a unified trajectory: sustained performance, verifiable regeneration (including the memory effect, where relevant), real water piloting, scalable supply, and regulatory standards consistent with the circular economy facilitate LDHs in progressing towards deployable technology for phosphorus management and recycling.[120,121]

Conclusions

Layered Double Hydroxides (LDH) materials are suitable candidates for water remediation, focusing on adsorbing phosphate anions from water. LDH materials possess an ionic lamellar structure, consisting of positively charged layers and negatively charged counterions or solvent molecules between them. This makes them a suitable alternative for oxoanion adsorption. Furthermore, LDH materials have been synthesized using numerous synthesis methods, including co-precipitation, urea hydrolysis, hydrothermal treatment, and sol–gel. The synthesis of LDHs is significantly influenced by the molar ratio of $M^{2+} : M^{3+}$, which facilitates the design of different materials using Zn, Mg, and Ca as the M^{2+} ions, and Al, Fe, and La as the M^{3+} ions, along with the design of magnetic and composite synthesis.

Different optimization parameters have been studied for phosphate adsorption, including dosage, contact time, the influence of pH and initial concentration, reusability, temperature, and the influence of co-existing ions. It is also evidenced that the major phosphate removal mechanisms are governed by a combination of processes, including electrostatic (ES) interactions, ion exchange (IE), ligand complexation (LC), layer expansion (LX), hydrogen bonding (HB), and π–π interactions. Moreover, LDH materials have displayed promising results for wastewater applications. They can be employed in both extreme and neutral pH conditions, exhibiting an outstanding adsorption capacity.

Thus, LDH materials have demonstrated sustained performance, verifiable regeneration (including the memory effect), successful real-world piloting, scalable supply, and regulatory standards aligned with the circular economy. These attributes facilitate the progression of LDHs towards a deployable technology for phosphorus management and recycling. Due to the above, LDHs possess a vast potential for phosphate remediation, which can significantly help solve the global issue of water eutrophication.

Conflicts of interest

There are no conflicts to declare.

Data availability

All data is available in the main text.

Acknowledgements

References

1 B. Moss, *Philos. Trans. R. Soc., B*, 2008, **363**, 659–666.

2 A. Ahamad, S. Madhav, A. K. Singh, A. Kumar and P. Singh, in *Sensors in Water Pollutants Monitoring: Role of Material*, ed. D. Pooja, P. Kumar, P. Singh and S. Patil, Springer Singapore, Singapore, 2020, pp. 21–41.

3 R. W. Howarth, A. Sharpley and D. Walker, *Estuaries*, 2002, **25**, 656–676.

4 B. Jiménez, *Irrig. Drain. Pap.*, 2005, **54**, S23–S33.

5 E. M. Bennett, S. R. Carpenter and N. F. Caraco, *BioScience*, 2001, **51**, 227.

6 L. De Jesús Velázquez-Chávez, J. A. Chávez-Simental, G. A. Pámanes-Carrasco, M. E. Pereda-Solís, A. Carrillo-Parra and I. A. Ortiz-Sánchez, *Ecol. Chem. Eng. S*, 2023, **30**, 373–386.

7 G. Alatrista, C. Pratt and A. El Hanandeh, *Chemosphere*, 2023, **339**, 139674.

8 L. Egle, H. Rechberger and M. Zessner, *Resour., Conserv. Recycl.*, 2015, **105**, 325–346.

9 J. L. Obeso, H. Viltres, C. V. Flores, V. B. López-Cervantes, C. Serrano-Fuentes, A. R. Rajabzadeh, S. Srinivasan, R. A. Peralta, I. A. Ibarra and C. Leyva, *RSC Appl. Interfaces*, 2024, **1**, 147–154.

10 W. Huang, Y. Zhang and D. Li, *J. Environ. Manage.*, 2017, **193**, 470–482.

11 Z. Wang, E. Nie, J. Li, M. Yang, Y. Zhao, X. Luo and Z. Zheng, *Environ. Sci. Pollut. Res.*, 2012, **19**, 2908–2917.

12 Q. Wang and D. O'Hare, *Chem. Rev.*, 2012, **112**, 4124–4155.

13 H. Boumeriame, E. S. Da Silva, A. S. Cherevan, T. Chafik, J. L. Faria and D. Eder, *J. Energy Chem.*, 2022, **64**, 406–431.

14 S. Anantharaj, K. Karthick and S. Kundu, *Mater. Today Energy*, 2017, **6**, 1–26.

15 M. Xu and M. Wei, *Adv. Funct. Mater.*, 2018, **28**, 1802943.

16 V. K. Ameena Shirin, R. Sankar, A. P. Johnson, H. V. Gangadharappa and K. Pramod, *J. Controlled Release*, 2021, **330**, 398–426.

17 A. Garcia-Gallastegui, D. Iuretagoyena, V. Gouvea, M. Mokhtar, A. M. Asiri, S. N. Basahel, S. A. Al-Thabaiti, A. O. Alyoubi, D. Chadwick and M. S. P. Shaffer, *Chem. Mater.*, 2012, **24**, 4531–4539.

18 H. Xu, S. Zhu, M. Xia and F. Wang, *J. Hazard. Mater.*, 2021, **402**, 123815.

19 X. Guo, P. Yin and H. Yang, *Microporous Mesoporous Mater.*, 2018, **259**, 123–133.

20 E. S. Behbahani, K. Dashtian and M. Ghaedi, *J. Hazard. Mater.*, 2021, **410**, 124560.

21 C. Wei, X. Yan, Y. Zhou, W. Xu, Y. Gan, Y. Zhang and N. Zhang, *Crystals*, 2022, **12**, 1713.

22 M. Richetta, P. G. Medaglia, A. Mattoccia, A. Varone and R. Pizzoferrato, *J. Mater. Sci. Eng.*, 2017, **6**(4), 1–9.

23 O. Hettithanthri, A. U. Rajapaksha, N. Nanayakkara and M. Vithanage, in *Novel Materials for Environmental Remediation Applications*, Elsevier, 2023, pp. 225–246.

24 A. Grover, I. Mohiuddin, A. K. Malik, J. S. Aulakh, K. Vikrant, K.-H. Kim and R. J. C. Brown, *J. Hazard. Mater.*, 2022, **424**, 127454.

25 Q. Zhou, M. Lei, J. Li, K. Zhao and Y. Liu, *Sep. Purif. Technol.*, 2017, **182**, 78–86.

26 S. Park, D. Kwon, J. Y. Kang and J. C. Jung, *Green Energy Environ.*, 2019, **4**, 287–292.

27 A. Farhan, A. Khalid, N. Maqsood, S. Iftekhar, H. M. A. Sharif, F. Qi, M. Sillanpää and M. B. Asif, *Sci. Total Environ.*, 2024, **912**, 169160.

28 D. Chaillot, S. Bennici and J. Brendlé, *Environ. Sci. Pollut. Res.*, 2021, **28**, 24375–24405.

29 L. H. Chagas, G. S. G. De Carvalho, W. R. Do Carmo, R. A. S. San Gil, S. S. X. Chiaro, A. A. Leitão, R. Diniz, L. A. De Sena and C. A. Achete, *Mater. Res. Bull.*, 2015, **64**, 207–215.

30 J. Tian, A. Zhang, R. Liu, W. Huang, Z. Yuan, R. Zheng, D. Wei and J. Liu, *J. Colloid Interface Sci.*, 2020, **579**, 607–618.

31 Y. Lin, X. Wang, J. Hao, P. Ning, G. Qu, L. Tang, Y. Xie, C. Du and Y. He, *Catal. Commun.*, 2019, **118**, 51–55.

32 M. Ogawa and S. Asai, *Chem. Mater.*, 2000, **12**, 3253–3255.

33 M. A. Farghali, A. M. Selim, H. F. Khater, N. Bagato, W. Alharbi, K. H. Alharbi and I. Taha Radwan, *Arabian J. Chem.*, 2022, **15**, 104171.

34 Z. Zhang, G. Chen and K. Xu, *Appl. Clay Sci.*, 2013, **72**, 206–210.

35 A. F. D. Silva, J. L. D. S. Duarte and L. Meili, *Sep. Purif. Technol.*, 2021, **264**, 118353.

36 D. Tichit, O. Lorret, B. Coq, F. Prinetto and G. Ghiotti, *Microporous Mesoporous Mater.*, 2005, **80**, 213–220.

37 P. Saikia, N. B. Allou, A. Borah and R. L. Goswamee, *Mater. Chem. Phys.*, 2017, **186**, 52–60.

38 A. O. Fadiran, S. C. Dlamini and A. Mavuso, *Bull. Chem. Soc. Ethiop.*, 2008, **22**, 197–206.

39 S. Haas, K. P. Sinclair and D. C. Catling, *Commun. Earth Environ.*, 2024, **5**, 28.

40 Q. Zhou, H. Sun, L. Jia, W. Wu and J. Wang, *Chemosphere*, 2022, **296**, 134054.

41 M. Forouzesh, E. Fatehifar, R. Khoshbouy and M. Daryani, *Chem. Eng. Res. Des.*, 2023, **189**, 308–318.

42 I. W. Almanassra, G. Mckay, V. Kochkodan, M. Ali Atieh and T. Al-Ansari, *Chem. Eng. J.*, 2021, **409**, 128211.

43 Y. Xi, M. Huang and X. Luo, *Appl. Surf. Sci.*, 2019, **467–468**, 135–142.

44 T. Liu, S. Zheng and L. Yang, *J. Colloid Interface Sci.*, 2019, **552**, 134–141.

45 L. Feng, Q. Zhang, F. Ji, L. Jiang, C. Liu, Q. Shen and Q. Liu, *Chem. Eng. J.*, 2022, **430**, 132754.

46 A. Drenkova-Tuhtan, K. Mandel, A. Paulus, C. Meyer, F. Hutter, C. Gellermann, G. Sextl, M. Franzreb and H. Steinmetz, *Water Res.*, 2013, **47**, 5670–5677.

47 R. Benhiti, A. Ait Ichou, A. Zaghloul, R. Aziam, G. Carja, M. Zerbet, F. Sinan and M. Chiban, *Environ. Sci. Pollut. Res.*, 2020, **27**, 45767–45774.

48 S. Mariska, Z. Jin-Wei, H. H. Chien, D. M. Ngoc, N. D. Hai and H.-P. Chao, *Appl. Water Sci.*, 2025, **15**, 42.

49 H. Hatami, A. Fotovat and A. Halajnia, *Appl. Clay Sci.*, 2018, **152**, 333–341.

50 S. Iftekhar, M. E. Küçük, V. Srivastava, E. Repo and M. Sillanpää, *Chemosphere*, 2018, **209**, 470–479.

51 K. Yang, L. Yan, Y. Yang, S. Yu, R. Shan, H. Yu, B. Zhu and B. Du, *Sep. Purif. Technol.*, 2014, **124**, 36–42.

52 C. V. Luengo, M. A. Volpe and M. J. Avena, *J. Environ. Chem. Eng.*, 2017, **5**, 4656–4662.

53 S. Qiu, D. Zhao, Y. Feng, M. Li, X. Liang, L. Zhang, Y. Luo, K. Zhang and F. Wang, *J. Environ. Manage.*, 2022, **303**, 114235.

54 Q. Zhang, F. Ji, T. Zhao, Q. Shen, D. Fang, L. Kuang, L. Jiang and S. Ding, *Appl. Clay Sci.*, 2019, **174**, 159–169.

55 M. Zhang, B. Gao, Y. Yao and M. Inyang, *Chemosphere*, 2013, **92**, 1042–1047.

56 Z. Lin and J. Chen, *Chemosphere*, 2021, **264**, 128551.

57 O. Alagha, M. S. Manzar, M. Zubair, I. Anil, N. D. Mu'azu and A. Qureshi, *Nanomaterials*, 2020, **10**, 1361.

58 S. Rahman, C. M. Navarathna, N. Krishna Das, J. Alchouron, P. Reneau, S. Stokes, R. V. K. G. Thirumalai, F. Perez, E. Barbary Hassan, D. Mohan, C. U. Pittman and T. Mlsna, *J. Colloid Interface Sci.*, 2021, **597**, 182–195.

59 P. Koilraj, C. A. Antonyraj, V. Gupta, C. R. K. Reddy and S. Kannan, *Appl. Clay Sci.*, 2013, **86**, 111–118.

60 I. A. Kumar and N. Viswanathan, *J. Chem. Eng. Data*, 2019, **64**, 5725–5736.

61 S. Li, J. Shao, B. Ma, B. Wu and C. Hu, *Chem. Eng. J.*, 2023, **464**, 142589.

62 F. Li, J. Jin, Z. Shen, H. Ji, M. Yang and Y. Yin, *J. Hazard. Mater.*, 2020, **388**, 121734.

63 S. Shan, X. Huang, Z. Yang, J. Ji, Z. Chen, C. Wang, X. Xu, X. Li, Y. Xu, S. Liu, B. Li and D. Li, *Process Saf. Environ. Prot.*, 2025, **199**, 107224.

64 H. Li, S. Cui, Y. Tan, Y. Peng, X. Gao, X. Yang, Y. Ma, X. He, B. Fan, S. Yang and Q. Chen, *Environ. Pollut.*, 2022, **294**, 118592.

65 X. Li, L. Xin, Y. Peng, S. Zhang, D. Guan and J. Song, *Magnetochemistry*, 2025, **11**, 27.

66 M. K. Motandi, Z. Zhang, S. Inkoua and L. Yan, *Environ. Prog. Sustainable Energy*, 2022, **41**, e13744.

67 R. Chitrakar, S. Tezuka, A. Sonoda, K. Sakane, K. Ooi and T. Hirotsu, *J. Colloid Interface Sci.*, 2007, **313**, 53–63.

68 O. Alagha, M. S. Manzar, M. Zubair, I. Anil, N. D. Mu'azu and A. Qureshi, *Nanomaterials*, 2020, **10**, 336.

69 P. Hu, Y. Zhang, F. Lv, W. Tong, H. Xin, Z. Meng, X. Wang and P. K. Chu, *Water Environ. J.*, 2017, **31**, 145–157.

70 Z. Qing, L. Wang, Q. Qin, C. Jiang, Z. Yang, Y. Liu, S. Zhang and J. Chen, *J. Water Process Eng.*, 2024, **59**, 104989.

71 Y.-T. Lai, W.-T. Liu, L.-J. Chen, M.-C. Chang, C.-Y. Lee and N.-H. Tai, *J. Mater. Chem. A*, 2019, **7**, 3962–3970.

72 N. Isidoro Ribeiro, O. Barreto Pessanha, M. Luiza Gomes Soares Pessanha and D. Guimarães, *Sep. Purif. Technol.*, 2023, **307**, 122717.

73 P. Karthikeyan and S. Meenakshi, *J. Mol. Liq.*, 2019, **296**, 111766.

74 C. Huang, C. Tang, Q. Wu and Q. Zhu, *Environ. Sci. Pollut. Res.*, 2022, **29**, 59224–59234.

75 P. Ma, J. Zhu, X. Du, Y. Yang, X. Hao, X. An, X. Hao and C. Prestigiacomo, *J. Colloid Interface Sci.*, 2022, **626**, 47–58.

76 P. Koilraj and K. Sasaki, *J. Environ. Chem. Eng.*, 2016, **4**, 984–991.

77 S. Cheng, L. Shao, J. Ma, X. Xia, Y. Liu, Z. Yang, C. Yang and S. Li, *Environ. Sci.: Nano*, 2019, **6**, 2615–2625.

78 J.-H. Kim, J.-K. Kang, S.-C. Lee and S.-B. Kim, *Appl. Clay Sci.*, 2019, **170**, 1–12.

79 A. Nuryadin, T. Imai, A. Kanno, K. Yamamoto, M. Sekine and T. Higuchi, *Mater. Chem. Phys.*, 2021, **266**, 124559.

80 W. Qiao, H. Bai, T. Tang, J. Miao and Q. Yang, *Colloids Surf., A*, 2019, **577**, 118–128.

81 Z. Qing, Q. Qin, L. Wang, C. Jiang, Z. Yang, Y. Liu, S. Zhang and J. Chen, *New J. Chem.*, 2024, **48**, 3208–3220.

82 D. Pattappan, S. Kapoor, S. S. Islam and Y.-T. Lai, *ACS Omega*, 2023, **8**, 24727–24749.

83 X. Li, B. Wang, Y. Cao, S. Zhao, H. Wang, X. Feng, J. Zhou and X. Ma, *ACS Sustainable Chem. Eng.*, 2019, **7**, 4548–4563.

84 D. Gao, W. Zhang, H. Dong, Y. Yu, W. Liu, H. Luo, Z. Jing, B. Liang, L. Peng, B. Wu, T. Huang and H. Cheng, *Environ. Technol. Innovation*, 2025, **37**, 104003.

85 O. Długosz and M. Banach, *Appl. Phys. A*, 2022, **128**, 919.

86 M. Adachi-Pagano, C. Forano and J.-P. Besse, *J. Mater. Chem.*, 2003, **13**, 1988–1993.

87 U. Costantino, N. Coletti, M. Nocchetti, G. G. Aloisi, F. Elisei and L. Latterini, *Langmuir*, 2000, **16**, 10351–10358.

88 H. Cai, A. C. Hillier, K. R. Franklin, C. C. Nunn and M. D. Ward, *Science*, 1994, **266**, 1551–1555.

89 U. Costantino, F. Marmottini, M. Nocchetti and R. Vivani, *Eur. J. Inorg. Chem.*, 1998, **1998**, 1439–1446.

90 E. M. Seftel, R. G. Ciocarlan, B. Michielsen, V. Meynen, S. Mullens and P. Cool, *Appl. Clay Sci.*, 2018, **165**, 234–246.

91 Q. Yu, Y. Zheng, Y. Wang, L. Shen, H. Wang, Y. Zheng, N. He and Q. Li, *Chem. Eng. J.*, 2015, **260**, 809–817.

92 D. L. Gao, W. W. Lin, Q. J. Lin, F. F. Dai, Y. X. Xue, J. H. Chen, Y. X. Liu, Y. Huang and Q. Yang, *J. Environ. Chem. Eng.*, 2023, **11**, 109472.

93 Z. Yang, C. Zhang, G. Zeng, X. Tan, H. Wang, D. Huang, K. Yang, J. Wei, C. Ma and K. Nie, *J. Mater. Chem. A*, 2020, **8**, 4141–4173.

94 Z. Yang, F. Wang, C. Zhang, G. Zeng, X. Tan, Z. Yu, Y. Zhong, H. Wang and F. Cui, *RSC Adv.*, 2016, **6**, 79415–79436.

95 J. Das, B. S. Patra, N. Baliarsingh and K. M. Parida, *Appl. Clay Sci.*, 2006, **32**, 252–260.

96 T. Hongo, T. Iemura and A. Yamazaki, *J. Ceram. Soc. Jpn.*, 2008, **116**, 192–197.

97 A. M. Cardinale, S. Vecchio Ciprioti, M. Fortunato and M. Catauro, *J. Therm. Anal. Calorim.*, 2023, **148**, 1523–1532.

98 A. M. Cardinale, M. Fortunato, F. Locardi and N. Parodi, *J. Therm. Anal. Calorim.*, 2022, **147**, 5297–5302.

99 B. Yang, D. Liu, J. Lu, X. Meng and Y. Sun, *Surf. Interface Anal.*, 2018, **50**, 378–392.

100 N. K. Gupta, M. Saifuddin, S. Kim and K. S. Kim, *J. Mol. Liq.*, 2020, **297**, 111935.

101 Q. He, H. Zhao, Z. Teng, Y. Wang, M. Li and M. R. Hoffmann, *Chemosphere*, 2022, **303**, 134987.

102 S. A. Raheem and A. A. Mohammed, *Results Surf. Interfaces*, 2025, **18**, 100386.

103 Y. Xu, Y. Yin, Y.-N. Luan, Q. Wang, Z. Zhao, Z. Guo and C. Liu, *Environ. Sci. Pollut. Res.*, 2024, **31**, 29132–29147.

104 H. Zhu, H. Ma, J. Yu, Z. Zhao, L. Xu, X. Li, Y. Rao, B. Lai and S. Pu, *ACS ES&T Water*, 2023, **3**, 3343–3356.

105 R. Long, Z. Yu, M. Shan, X. Feng, X. Zhu, X. Li and P. Wang, *Colloids Surf., A*, 2022, **634**, 127942.

106 V. Prevot and E. Bourgeat-Lami, in *Layered Double Hydroxide Polymer Nanocomposites*, Elsevier, 2020, pp. 461–495.

107 R. Zhao, T. Ma, S. Zhao, H. Rong, Y. Tian and G. Zhu, *Chem. Eng. J.*, 2020, **382**, 122893.

108 Z. Zheng, Z. Li, Z. Hu, J. Zhang, Y. Wang, Y. Xu and T. Li, *J. Environ. Chem. Eng.*, 2024, **12**, 114289.

109 Y. Liu, H. Li, K. Cui, P. Liu, J. Guo, J. Yi, D. Feng, R. Gong and J. Fu, *J. Chem. Technol. Biotechnol.*, 2025, **100**, 1920–1929.

110 T. Sheng, Z. Zhang, Y. Hu, Y. Tao, J. Zhang, Z. Shen, J. Feng and A. Zhang, *Environ. Sci. Pollut. Res.*, 2019, **26**, 7102–7114.

111 M. Sürmeli, H. Yazıcı, M. Kılıç and M. Karaboyacı, *J. Water Process Eng.*, 2022, **49**, 103001.

112 K. Sheoran, H. Kaur, S. S. Siwal, A. K. Saini, D.-V. N. Vo and V. K. Thakur, *Chemosphere*, 2022, **299**, 134364.

113 K. Alqudaihi, B. Alrwaily, B. Alzawad, M. Sheraz, M. Zubair, Z. Arshad, I. Hussain, M. A. Aziz and N. Baig, *Chem.–Asian J.*, 2025, e00445.

114 C. Chen, L. Tao, S. Du, W. Chen, Y. Wang, Y. Zou and S. Wang, *Adv. Funct. Mater.*, 2020, **30**, 1909832.

115 P. S. Kumar, L. Korving, M. C. M. Van Loosdrecht and G.-J. Witkamp, *Water Res.:X*, 2019, **4**, 100029.

116 D. Fang, L. Huang, H. Xiao, G. Wu, Z. Zeng, X. Wang, G. Yang, F. Shen, S. Deng and F. Ji, *Chem. Eng. J.*, 2023, **451**, 138600.

117 T. Zhang, Z. Xu, Z. Xu, Y. Ma, Z. Niu, J. Chen, M. Zhang and F. Shi, *Environ. Res.*, 2025, **271**, 121031.

118 S. Sarkar and C. Upadhyay, *Catal. Today*, 2025, **445**, 115101.

119 B. M. V. D. Gama, R. Selvasembian, D. A. Giannakoudakis, K. S. Triantafyllidis, G. McKay and L. Meili, *Molecules*, 2022, **27**, 4900.

120 I. Clark, R. L. Gomes, C. Crawshaw, L. Neve, R. Lodge, M. Fay, C. Winkler, M. Hull and E. Lester, *React. Chem. Eng.*, 2019, **4**, 663–666.

121 A. Seijas-Da Silva, A. Hartert, V. Oestreicher, J. Romero, C. Jaramillo-Hernández, L. J. J. Muris, G. Thorez, B. J. C. Vieira, G. Ducourthial, A. Fiocco, S. Legendre, C. Huck-Iriart, M. Mizrahi, D. López-Alcalá, A. T. S. Freiberg, K. J. J. Mayrhofer, J. C. Waerenborgh, J. J. Baldoví, S. Cherevko, M. Varela, S. Thiele, V. Lloret and G. Abellán, *Nat. Commun.*, 2025, **16**, 6138.

122 C. Dazon, C. Taviot-Guého and V. Prévot, *Mater. Adv.*, 2023, **4**, 4637–4645.

123 Z. Yin, W. Zhao, Y. Sun, G. Wang, T. Ma, J. Sun and P. Ji, *Chem. Eng. J.*, 2025, **520**, 165828.

124 A. U. Kura, M. Z. Hussein, S. Fakurazi and P. Arulselvan, *Chem. Cent. J.*, 2014, **8**, 47.

125 M. Laipan, J. Yu, R. Zhu, J. Zhu, A. T. Smith, H. He, D. O'Hare and L. Sun, *Mater. Horiz.*, 2020, **7**, 715–745.

126 C. Delhoyo, *Appl. Clay Sci.*, 2007, **36**, 103–121.

127 Z. Zhou, D. Luo, X. Zhang and C. Wang, *Ind. Crops Prod.*, 2025, **224**, 120422.

128 M. Sürmeli and H. Yazıcı, *Water, Air, Soil Pollut.*, 2025, **236**, 15.

129 H. Ye, S. Liu, D. Yu, X. Zhou, L. Qin, C. Lai, F. Qin, M. Zhang, W. Chen, W. Chen and L. Xiang, *Coord. Chem. Rev.*, 2022, **450**, 214253.

130 M. Li, T. Chowdhury, A. N. Kraetz, H. Jing, A. Dopilka, L. M. Farmen, S. Sinha and C. K. Chan, *ChemEngineering*, 2019, **3**, 20.

131 A. Singha Roy, S. Kesavan Pillai and S. S. Ray, *ACS Omega*, 2022, **7**, 20428–20440.

132 A. F. Da Silva, J. L. Da Silva Duarte, R. Selvasembian and L. Meili, *J. Nanopart. Res.*, 2023, **25**, 16.

133 K. Bisaria, C. S. Seth and R. Singh, *Environ. Sci.: Adv.*, 2024, **3**, 1153–1162.

134 K. Lin, X. Feng, N. Zhang, K. Song, Y. Yao, R. Jiao, Y. Chen, L. Shi and J.-W. Shi, *Sci. China Chem.*, 2025, **68**, 4642–4676.

135 C. Jing, B. Dong and Y. Zhang, *Energy Environ. Mater.*, 2020, **3**, 346–379.

136 A. A. Altalhi, E. A. Mohamed and N. A. Negm, *Energy Adv.*, 2024, **3**, 2136–2151.

137 K. Rybka and J. Matusik, *J. Cleaner Prod.*, 2025, **498**, 145215.

138 Y. Chen, H. Xu, M. S. Khan, S. Han and S. Zhu, *Crit. Rev. Environ. Sci. Technol.*, 2025, **55**, 1097–1123.

139 L. Min, J. Duan, L. Liu, S. Ge, W. Zhang and Y. Wang, *Dalton Trans.*, 2022, **51**, 2033–2040.